nature neuroscience

Article

https://doi.org/10.1038/s41593-024-01791-4

Astrocyte transcriptomic changes along the spatiotemporal progression of Alzheimer's disease

Received: 11 November 2022

Accepted: 17 September 2024

Published online: 11 November 2024

Check for updates

Alberto Serrano-Pozo[1,2,3,7], Huan Li[1,3,7], Zhaozhi Li[1,7], Clara Muñoz-Castro[1,3], Methasit Jaisa-aad[1,3], Molly A. Healey[1], Lindsay A. Welikovitch[1,3], Rojashree Jayakumar[1], Annie G. Bryant[1], Ayush Noori[1], Theresa R. Connors[1,2], Miwei Hu[1], Karen Zhao[4], Fan Liao[4], Gen Lin[5], Timothy Pastika[4], Joseph Tamm[4], Aicha Abdourahman[4], Taekyung Kwon[4], Rachel E. Bennett[1,3], Maya E. Woodbury[4], Astrid Wachter[5], Robert V. Talanian[4], Knut Biber[6], Eric H. Karran[4], Bradley T. Hyman[1,2,3] & Sudeshna Das[1,2,3]

Astrocytes are crucial to brain homeostasis, yet their changes along the spatiotemporal progression of Alzheimer's disease (AD) neuropathology remain unexplored. Here we performed single-nucleus RNA sequencing of 628,943 astrocytes from five brain regions representing the stereotypical progression of AD pathology across 32 donors spanning the entire normal aging to severe AD continuum. We mapped out several unique astrocyte subclusters that exhibited varying responses to neuropathology across the AD-vulnerable neural network (spatial axis) or AD pathology stage (temporal axis). The proportion of homeostatic, intermediate and reactive astrocytes changed only along the spatial axis, whereas two other subclusters changed along the temporal axis. One of these, a trophic factor-rich subcluster, declined along pathology stages, whereas the other increased in the late stage but returned to baseline levels in the end stage, suggesting an exhausted response with chronic exposure to neuropathology. Our study underscores the complex dynamics of astrocytic responses in AD.

Alzheimer's disease (AD) is defined by the widespread accumulation of amyloid-β (Aβ) plaques and phospho-tau (pTau) neurofibrillary tangles (NFTs) throughout the brain, with the latter following a stereotypical hierarchical spatiotemporal pattern along neural networks. These AD neuropathological changes (ADNC) are accompanied by a dramatic loss of synapses and neurons, as well as prominent morphological and functional changes of glial cells, collectively termed reactive gliosis[1]. Astrocytes are critical for maintaining brain homeostasis[2], and the emerging view from experimental data is that reactive astrogliosis may contribute to neurodegeneration through both gains of toxic functions and loss of normal functions[1]. Indeed, numerous astrocyte-specific transcriptomic studies in various transgenic mouse models of AD[3–8] have supported this view. Recent single-nucleus RNA-sequencing (snRNA-seq) studies[9–17] have begun to unravel the molecular underpinnings of reactive astrocytes in the human AD brain as well, but several questions remain—(1) are there regional differences in astrocyte gene expression in the normal aging brain? (2) What are the gene expression changes that astrocytes exhibit along the spatiotemporal progression

[1]Massachusetts General Hospital, Department of Neurology, Boston, MA, USA. [2]Massachusetts Alzheimer's Disease Research Center, Charlestown, MA, USA. [3]Harvard Medical School, Boston, MA, USA. [4]AbbVie, Cambridge Research Center, Cambridge, MA, USA. [5]AbbVie Deutschland GmbH & Co. KG, Genomics Research Center, Ludwigshafen, Germany. [6]AbbVie Deutschland GmbH & Co. KG, Neuroscience Research, Ludwigshafen, Germany. [7]These authors contributed equally: Alberto Serrano-Pozo, Huan Li, Zhaozhi Li. e-mail: sdas5@mgh.harvard.edu

of AD, and how does the severity of ADNC affect the astrocyte transcriptome? (3) Are there different astrocyte transcriptional subpopulations or dynamic states in the AD brain? We addressed these questions by conducting a large snRNA-seq study in five brain regions from 32 control and AD donors with various degrees of ADNC, allowing us to unravel the consequences of the hierarchical progression of AD for astrocyte biology.

Results

A molecular survey of astrocytes in five brain regions affected stereotypically in AD

Using an enrichment strategy consisting of depleting NeuN-positive neurons and OLIG2-positive oligodendrocytes via fluorescence-activated nuclei sorting (FANS)[18,19] (Fig. 1a and Supplementary Fig. 1a), we obtained a total of 628,943 astrocyte nuclei from five brain regions of 32 individuals with autopsy findings along the normal aging to severe AD neuropathological continuum (Fig. 1a). The five brain regions were selected to represent the hierarchical spreading of pTau NFTs along brain networks as categorized by the Braak NFT staging system[20,21] and included entorhinal cortex (EC), inferior temporal gyrus (ITG, Brodmann area (BA) 20), dorsolateral prefrontal cortex (PFC, BA46), secondary (association) visual cortex (V2, BA18/19) and primary visual cortex (V1, BA17). Our strategy to enrich astrocyte nuclei was effective, as indicated by the low numbers of neuronal and oligodendroglial nuclei identified (Fig. 1b). Astrocyte nuclei were identified by the expression levels of the marker genes *ADGRV1* (refs. 13,22), *ALDH1L1*, aquaporin-4 (*AQP4*) and *GFAP* (Fig. 1c), resulting in over 100,000 astrocyte nuclei in each brain region with ≈6,000 average total number of reads and ≈2,500 average total number of genes detected, which is orders of magnitude higher than previous studies[9–15] (Supplementary Fig. 1b).

Because astrocyte morphology changes near Aβ plaques and pTau NFTs[23,24], we quantified the local burden of ADNC in adjacent tissue samples by measuring the 3D6-positive Aβ-immunoreactive percentage area fraction via immunohistochemistry and the pTau/total tau ratio via ELISA. To reflect the progression of ADNC, we then grouped the 32 donors into four pathology stages based on their global semiquantitative measures of neuritic plaques (Consortium to Establish a Registry for Alzheimer's Disease (CERAD) neuritic plaque (NP) score) and NFTs (Braak NFT stages) complemented with these immunohistochemical and biochemical quantitative measures of local Aβ and pTau burdens. The four pathology stages were as follows: (1) not AD/low ADNC burden (no NPs, Braak NFT stages 0/I/II), (2) intermediate ADNC burden (sparse or moderate NPs and Braak NFT stages II/III), (3) high ADNC burden with moderate or frequent NPs and Braak NFT stage V and (4) high ADNC burden with moderate or frequent NPs and Braak NFT stage VI. We separated the latter two groups because, by definition, the primary visual cortex (V1 region) bears NFTs only in Braak NFT stage VI[20,21]. Figure 1d illustrates the quantitative measures of ADNC across brain regions of the 32 donors grouped in these four pathological stages. Within each stage, the Aβ plaque load was relatively constant across brain regions except for higher levels in PFC at late stages. By contrast, the pTau/tau ratio was highest in EC and demonstrated the expected pattern EC > ITG > PFC > V2 > V1 across all stages, consistent with the stereotypical hierarchical accumulation of NFTs along neural networks[20,21] (Fig. 1d and Supplementary Fig. 1c). The demographic and neuropathological characteristics of the study donors, including quantitative measures of Aβ and pTau, are summarized in Table 1 and detailed in Supplementary Data 1.

Regional heterogeneity of astrocyte transcriptome in the normal aging brain

Numerous transcriptomics studies have described the region-specific diversity of astrocytes in the mouse[8,25–32], but less is known about the transcriptomic heterogeneity of astrocytes across different cortical areas in the aging human brain. Our eight control donors provided a unique opportunity to examine regional differences in the astrocyte transcriptome in the normal aging brain because these donors had essentially no 3D6-positive Aβ plaques across the five brain regions and very low pTau/tau ratios except for the EC, as expected in Braak NFT stages 0/I/II (Fig. 1d). Thus, we asked whether the astrocyte transcriptome varies across regions in the normal aging brain. To address this question, we integrated a total of 246,464 nuclei from all brain regions of these eight individuals and conducted a differential gene expression analysis of each brain region relative to all other regions (Supplementary Data 2). Remarkably, the EC and V1 regions had the highest number of differentially expressed genes (DEGs; EC: 137 up and 152 down; V1: 93 up and 122 down; see Venn diagrams in Fig. 2a). A heatmap with relevant DEGs per region is shown in Fig. 2b. Among other genes of interest, *APOE*, *APP*, *AQP4* and *GJA1* were upregulated, whereas *ALDH1L1*, *LRP1B*, microtubule-associated protein tau (*MAPT*) and *SLC1A2* were downregulated in EC relative to the other brain regions. Conversely, *CLU*, *GFAP* and *MAOB* were upregulated, whereas *AQP4* and *GJA1* were downregulated in V1 versus all other brain regions. Validation with immunohistochemistry confirmed the regional differences between EC and V1 for *AQP4* and *GJA1* at the protein level (Fig. 2c and Supplementary Figs. 2 and 3).

These results suggest some degree of region-specificity of astrocyte transcriptome in the allocortex (EC) versus primary neocortex (V1) versus association neocortex (ITG, PFC and V2). To further examine this possibility, we asked whether EC DEGs are driven by the EC microenvironment (that is, allocortex versus neocortex) or by the amount of local EC pTau pathology already present in Braak stages I and II donors (Fig. 1d and Supplementary Data 2). First, we identified a gene set associated with the local pTau burden by regressing gene expression levels against the pTau/tau ratio across all five brain regions in these eight donors (148 positively and 433 negatively correlated genes, false discovery rate (FDR) < 0.05; Supplementary Data 3 and volcano plot in Fig. 2d). Then, to disambiguate EC-specific versus pTau-driven genes, we overlapped these pTau-correlated genes with those enriched in the EC (see Venn diagrams in Fig. 2e). Only 18 of the 137 EC-upregulated genes were positively correlated with the pTau/tau ratio (notably including cytoskeletal genes such as *MAP2* and the master transcription factor regulating cholesterol metabolism, *SREBF1*), whereas only 37 of 152 EC-downregulated genes were negatively correlated with the pTau/tau ratio (including extracellular matrix/glycosaminoglycan metabolism genes, such as *LARGE1* and *PTN*). Taken together, these results support the existence of an allocortex-specific gene expression profile in EC astrocytes, which is distinct from a pTau signature.

Astrocyte transcriptomic changes along the stereotypical spatial progression of AD

Next, we examined whether astrocyte gene expression changes track with the stereotypical spatiotemporal progression of AD neuropathology. The present study design with 32 donors along the normal aging to severe AD continuum and five sites that are hierarchically involved in stereotypical AD enabled us to address the hypothesis that the magnitude of astrocyte transcriptomic changes would parallel both the regional vulnerability of neural networks to ADNC (spatial progression) and the temporal accrual of ADNC in a given brain region (temporal progression).

First, to determine whether astrocyte transcriptomic changes follow the neural network predilection of AD progression, we rank ordered the five brain regions based on their known vulnerability to neurofibrillary degeneration[20,21] (that is, EC > ITG > PFC > V2 > V1) and performed a differential expression analysis comparing each node of the network with the next (that is, EC versus ITG, ITG versus PFC, PFC versus V2 and V2 versus V1), including all 32 donors and controlling for within-donor correlations. The resulting 504 DEGs between any two adjacent network nodes were then grouped into six spatial gene sets following distinct trajectories along the neural network (Fig. 3a and

https://doi.org/10.1038/s41593-024-01791-4

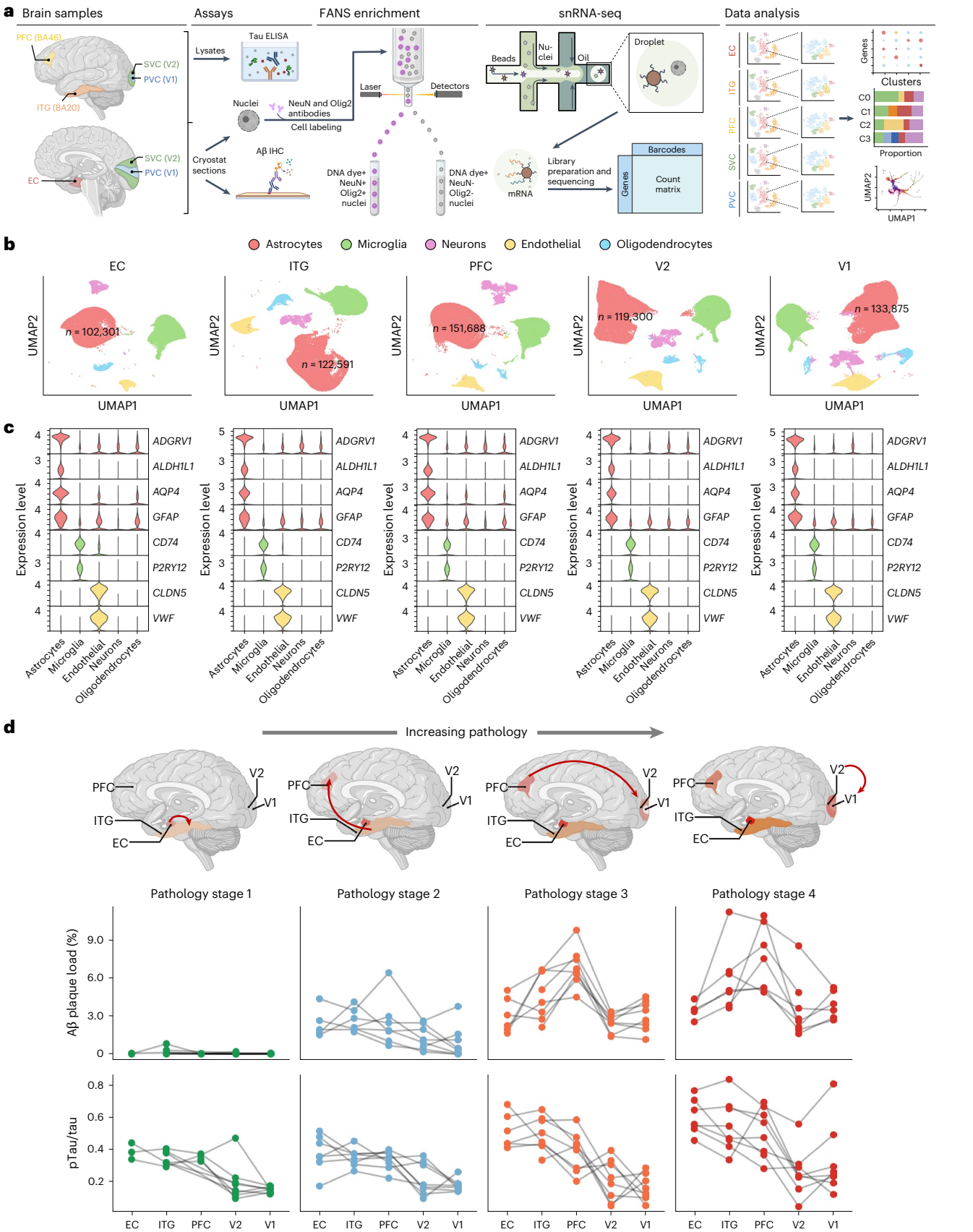

Fig. 1 | A molecular survey of astrocytes in five brain regions affected stereotypically in AD. a, Experimental overview of our snRNA-seq study. The figure was created with BioRender.com **b**, UMAP visualization showing clustering of NEUN$^-$/OLIG2$^-$ nuclei. **c**, Violin plots illustrate the expression levels of cell type-specific marker genes in NEUN$^-$/OLIG2$^-$ nuclei across the five brain regions. **d**, Results of Aβ plaque load (percentage of immunoreactive area fraction) and pTau/tau ratio (measured by ELISA) in adjacent samples to those used for snRNA-seq across brain regions and pathology stages. SVC, secondary (association) visual cortex; PVC, primary visual cortex; IHC, immunohistochemistry; FANS, fluorescence-activated nuclei sorting.

Table 1 | Donor summary characteristics

Summary	Pathology stage 1	Pathology stage 2	Pathology stage 3	Pathology stage 4
Age at death (mean±s.d.)	79.5±12.3	86±6.6	82.875±7.9	79.5±10.4
Sex, *n* (% female)	4 (50)	5 (62.5)	6 (75)	4 (50)
APOE ε4 carriers, *n* (%)	0 (0)	0 (0)	3 (37.5)	4 (50)
Braak NFT stages	0/I/II	II/III	V	VI
CERAD NP scores	None	Sparse or moderate	Moderate or frequent	Moderate or frequent
Aβ plaque burden (mean±s.d.)	0.070±0.152	1.855±1.384	4.072±2.103	4.909±2.536
EC	0.031±0.036	2.420±1.153	3.072±1.380	3.484±0.571
ITG	0.192±0.274	2.513±0.845	4.662±1.842	5.938±2.568
PFC	0.018±0.010	2.448±1.900	6.869±1.539	7.556±2.544
V2	0.040±0.061	1.271±0.943	2.467±0.701	3.524±2.278
V1	0.021±0.019	0.908±1.277	3.039±1.180	3.894±1.072
pTau/tau (mean±s.d.)	0.257±0.114	0.286±0.109	0.343±0.178	0.443±0.204
EC	0.385±0.051	0.374±0.114	0.512±0.107	0.600±0.109
ITG	0.343±0.043	0.347±0.056	0.494±0.104	0.547±0.162
PFC	0.348±0.021	0.333±0.058	0.383±0.124	0.505±0.152
V2	0.193±0.119	0.212±0.100	0.208±0.128	0.256±0.147
V1	0.150±0.017	0.175±0.038	0.162±0.079	0.328±0.221

Demographics, *APOE* genotype and neuropathology of donors are presented across the different stages of pathology. Summary statistics for Aβ plaque burden and the pTau/tau ratio for each brain region are also reported.

Supplementary Data 4). Two spatial gene sets changed their expression level monotonically along the network, either decreasing from EC to V1 (gene set 1) or increasing from EC to V1 (gene set 2). Two other spatial gene sets had relatively stable expression levels across all brain regions, except for a peak of upregulation (gene set 3) or downregulation (gene set 4) at the PFC. The last two spatial gene sets exhibited relatively constant expression levels in EC, ITG and PFC, but either decreased (gene set 5) or increased (gene set 6) from the PFC to V2 and V1. Thus, this analysis suggested a significant association between astrocyte gene expression and relevant regions that are hierarchically affected by the AD pathophysiological process. A heatmap depicting the differential expression of the individual genes comprising these spatial gene sets across brain regions at the individual donor level is shown in Supplementary Fig. 4a, demonstrating remarkable consistency with the average profile of these gene sets shown in Fig. 3a. Donor-level expression of representative genes for each spatial trajectory is shown in Supplementary Fig. 4b.

Previous transcriptomic studies comparing AD mouse models have reported similarities and differences in astrocyte responses to Aβ plaques versus pTau NFTs[5,7,33]. To test whether the spatial trajectories of astrocyte gene expression are also related to local Aβ and pTau levels, we correlated the average standardized expression of each of these spatial gene sets for each brain region and donor with the Aβ plaque burden and the pTau/tau ratio measured in the same brain regions and donors, while controlling for within-donor correlation (Fig. 3b and Supplementary Fig. 4c). Interestingly, the gene set decreasing linearly from EC to V1 (gene set 1) was positively correlated with the pTau/tau ratio, whereas the one increasing from EC to V1 (gene set 2) was negatively correlated with the pTau/tau ratio, suggesting that these two gene sets contain a pTau-associated signature. Gene set 1 contained synapse-associated (*GRIA1*, *GRIP1*, *KCND2*, *KCNE4*, *KCNN3*, *SYNPO2* and *SYTL4*), cell–cell communication (*APP*, *AQP4*, *CNTN1*, *IL33*, *ITGB4* and *TJP2*), cytoskeleton (*GSN*, *MAP2*, *MAP7*, *MYBPC1*, *TLN2* and *TTN*), extracellular matrix (*ADAMTSL3*, *COL21A1*, *LAMA4*, *SERPINI2* and *VCAN*) and some trophic factors (*ANGPT1*, *EGF*, *NRP2* and *NTRK2*), metal binding (*CP* and *FTH1*) and lipid metabolism (*ABCA1* and *LRAT*) genes, whereas gene set 2 included genes involved in glutamate neurotransmission (*GLUL*, *GRIA2*, *NRXN1* and *SLC1A2*) and extracellular matrix (*ADAM12*, *FREM2*, *MGAT5* and *PTN*; Fig. 3c).

By contrast, the gene set specifically upregulated at the PFC (gene set 3) was only positively correlated with the Aβ plaque burden, which was highest in this brain region (Fig. 1d), suggesting that this is an Aβ-associated signature. This gene set was enriched in synapse-associated (*DISC1*, *GRIA4*, *GRID2* and *SYNDIG1*), cell–cell communication (*APBB1IP*, *EFNA5*, *EPHA6* and *SPP1*) and cytoskeletal (*SYNM* and *FMN1*) genes that were distinct from those associated with the pTau/tau ratio (Fig. 3c). On the other hand, the gene set specifically downregulated in the PFC (gene set 4) contained important genes involved in cytoskeleton (*ACTB*, *CAP2*, *GFAP*, *MAP1B* and *VIM*), lipid metabolism (*APOE*, *CLU* and *DGKB*) and calcium homeostasis (*CALM2*, *CNN3*, *RTN1*, *S100A1* and *S100B*), as well as many extracellular matrix (*CST3*, *KAZN*, *HS6ST3*, *LAMA2*, *MATN2*, *SDC4*, *SERPINA3*, *SERPINH1*, *SPARC* and *TNC*), proteostasis (*BAG3*, *CRYAB*, *DNAJA1*, *DNAJB1*, *HSP90AA1*, *HSPA1A*, *HSPA1B*, *HSPB1*, *HSPB8*, *HSPD1*, *HSPE1*, *HSPH1*, *UBB* and *UBC*) and antioxidant defense genes (*PRDX1*, *SOD2* and the metallothioneins *MT1E*, *MT1F*, *MT1G*, *MT1M*, *MT1X*, *MT2A*, *MT1M*, *MT2A* and *MT3*; Fig. 3c). While this gene set was negatively correlated with both Aβ plaque burden and pTau/tau ratio, the statistical significance was lost after controlling for brain region.

Finally, spatial gene set 5 was positively correlated with both pTau/tau ratio and Aβ plaque burden, whereas gene set 6 was negatively correlated with both measures, likely representing ADNC-associated pan-reactive upregulated and downregulated signatures, respectively. The pan-reactive genes positively correlated with pTau and Aβ levels included many genes involved in G-protein-coupled receptor (GPCRs) signaling (*ARHGEF12*, *GNA14*, *GNAQ*, *PDE3B*, *PDE4D*, *PDE4DIP*, *PDE5A* and *PRKG1*) and intracellular transport (*CPQ*, *DNAH7*, *DNM3*, *RANBP3L*, *SLC1A3*, *SLC15A2*, *SLC44A3* and *SLCO1C1*), suggesting activation of second messenger-mediated signaling cascades and intracellular trafficking of solutes and vesicles (Fig. 3c). Remarkably, the pan-reactive genes negatively correlated with pTau and Aβ levels were predominantly related to cell motility (*ACTN*, *ASAP3*, *CXCL14*, *DAAM2*, *MYH9* and *SERPINE2*) and metabolism, including glucose (*ALDH1A1*, *DPP6*, *GAPDH*, *GYS1*, *LDHB* and *MIDN*), lipid (*ABHD3*, *OSBPL3* and *SLC27A1*) and

https://doi.org/10.1038/s41593-024-01791-4

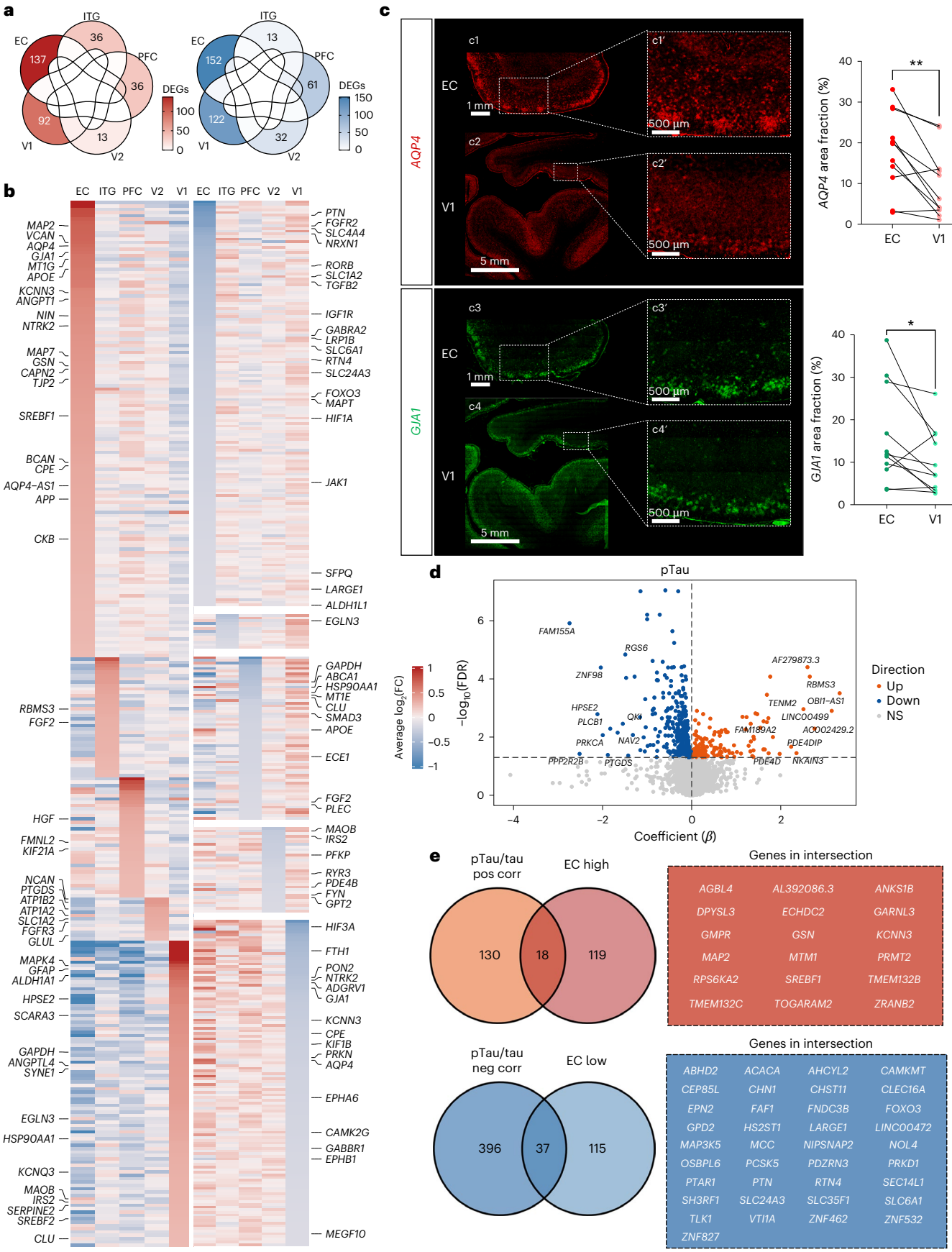

Fig. 2 | Regional heterogeneity of astrocyte transcriptome in the normal aging brain. a, Venn diagrams show the DEGs—upregulated in red and downregulated in blue—in each brain region relative to all other brain regions in $n = 8$ donors at pathology stage 1 (no neuritic plaques and Braak NFT stages 0/I/II). **b**, Heatmap depicts the DEGs in each brain region (upregulated in red and downregulated in blue) ranked by average log FC. **c**, Fluorescence immunohistochemistry of *AQP4* and connexin-43 (*GJA1*) in EC and V1. Automated immunohistochemistry with the peroxidase-DAB method followed by quantification of *AQP4*- and *GJA1*-immunoreactive percentage area fraction in EC and V1 formalin-fixed paraffin-embedded (FFPE) sections from $n = 11$ pathology stage 1 donors (including two donors from this snRNA-seq study) demonstrated a higher expression of these two proteins in EC versus V1, in agreement with the snRNA-seq results. $^{*}P = 0.05$, $^{**}P = 0.0036$, two-sided paired t test. Scale bars—EC, 1 mm; V1, 5 mm; insets, 500 µm. **d**, Volcano plot illustrates the correlation analysis between pTau/tau ratio and astrocyte gene expression levels in pathology stage 1 donors. The x axis represents the correlation coefficient β, while the y axis indicates the FDR (expressed as $-\log_{10}$(FDR)). Genes in red are positively correlated, and those in blue are negatively correlated at an FDR < 0.05 ($-\log_{10}$(FDR) > 1.3), whereas genes in gray were statistically NS. **e**, Venn diagrams show the number of genes upregulated in EC (EC high) and/or positively correlated with the pTau/tau ratio (top) and the number of genes downregulated in EC (EC low) and/or genes negatively correlated with pTau/tau ratio (bottom). Genes in each intersection are listed in the boxes. NS, not significant.

nucleotide (*DHFR*) pathways, suggesting a failure of energy metabolism in reactive astrocytes associated with chronic exposure to both pTau and Aβ (Fig. 3c).

We then asked whether this association could be driven by the regional differences observed in normal control donors or whether it was mainly explained by the accumulation of Aβ and/or pTau in those brain regions. To test the first possibility, we compared the EC-specific and V1-specific signatures obtained from normal controls (Fig. 2) and these spatial trajectory gene sets derived from the entire sample and, indeed, observed a significant overlap (Supplementary Fig. 4d). Specifically, the gene set with monotonic decrease from EC to V1 (gene set 1) was significantly enriched in EC-high and V1-low genes, whereas the gene set with monotonic increase from EC to V1 (gene set 2) was significantly enriched in EC-low and V1-high genes. The gene set specifically upregulated in PFC (gene set 3) was not enriched in either EC or V1 signatures, whereas the gene set specifically downregulated in PFC was enriched in EC-high and V1-high genes. The gene set with relatively stable expression in EC through PFC and lower expression in V2 and V1 (gene set 5) was enriched in EC-low and V1-low genes, and the gene set with stable levels in EC through PFC but increase in V2 and V1 (gene set 6) was expectedly enriched in V1-high genes (Fig. 3b). These data suggest that some of the regional variations in astrocyte transcriptome along the AD neural network are already present in the normal aging brain, possibly driven by exposure of astrocytes to microenvironmental factors particular to each brain region.

Taken together, these results indicate that the astrocyte gene expression profile parallels the typical spatial progression of AD pathology along neural networks and suggest that these astrocyte transcriptomic changes are partly associated with the local levels of Aβ plaques and/or pTau and partly explained by region-specific microenvironmental factors.

Astrocyte transcriptomic changes along the temporal progression of AD

Once we established the spatial progression of astrocyte transcriptomic changes in the normal aging to severe AD continuum, we sought to determine whether astrocyte transcriptomic changes also parallel the temporal accrual of ADNC within a given brain region. To this end, we conducted a differential expression analysis comparing each of the aforementioned four pathology stages with the next while controlling for brain region and within-donor correlation. We decided to separate Braak stages V and VI donors to investigate possible end-stage changes in astrocyte transcriptome and because, by definition, the primary visual cortex (V1) only contains NFTs in Braak stage VI donors but is spared from NFTs in Braak stage V donors[20,21]. The resulting 798 DEGs between any two adjacent stages were, thus, considered temporally associated with AD pathophysiology. These 798 DEGs were grouped into six different temporal gene sets with distinct temporal trajectories and variable strength of association with the local Aβ and pTau levels (Fig. 4 and Supplementary Data 5).

One set (temporal gene set 1) had the highest expression at an early stage (no NPs, Braak NFT stages 0/I/II) and then decreased and remained relatively low along all the other stages, suggesting that it corresponds to a homeostatic signature of astrocytes. This gene set included many trophic factors and their receptors (*ANGPTL4*, *APC*, *EGLN3*, *FGF2*, *GFRA1*, *HGF*, *IGF1R*, *NRP1*, *NTRK3*, *TGFB2*, *TGFBR3* and *VEGFA*), extracellular matrix (*GPC4*, *MATN2*, *SERPINA3*, *SERPINE2* and *SPOCK1*), cytoskeleton (*ACTN1*, *FIGN*, *MACF1*, *MAPRE2*, *MAST4* and *MYH9*) and some metal binding (*CP*, *FTL* and *MT2A*), antioxidant (*MGST1* and *MSRA*) but also pro-oxidant enzymes (*MAOB*), neuroinflammation (*MAP3K14*, *MAP4K4*, *OSMR*, *SOCS3* and *TAB2*), calcium homeostasis (*CALN1*, *CNN3* and *S100A1*) and phagocytosis (*LGALS3* and *SCARA3*) genes.

Another gene set (gene set 2) peaked at the intermediate ADNC stage (sparse/moderate NPs and Braak NFT stage II/III) and then returned to baseline at late and end stages, suggesting a transient activation of this gene set in response to the initial accumulation of ADNC. This early gene program included trophic and survival factors (*FGF1*, *FGF14*, *HIF1A* and *NRP2*), extracellular matrix (*GPC6*, *KAZN*, *LAMA4* and *TNC*), cytoskeleton (*ABI1*, *CLIP1*, *MYO1E* and *VCL*) and neuroinflammation (*CHI3L1*, *IFI16*, *IL1R1*, *IL6R* and *RCAN1*) genes, which differ from those predominant in the early ADNC stage. It also encompassed genes involved in lipid metabolism (*ACSL3*, *ELOVL5*, *ELOVL6*, *LDLR*, *LEPR*, *LPIN1*, *NCEH1*, *OSBPL6*, *PLA2G4C*, *PLCL1*, *PLPP3* and *SGMS2*), glycosaminoglycan metabolism (*EXT1*, *GALNT2*, *MAN2A1*, *ST6GALNAC3*, *SULF1* and *UGP2*), synapse-associated (*GRIK2*, *PCLO*, *STXBP6* and *SYTL2*) and GPCR-mediated signaling (*GPR158*, *KALRN*, *PDE4B*, *PDE4D*, *RASGEF1B*, *RGS6* and *TRIO*).

Two other temporal gene sets either peaked (gene set 3) or dropped (gene set 4) at the late stage (moderate/frequent NPs, Braak NFT stage V) but surprisingly returned to near baseline at end stage (moderate/frequent NPs, Braak NFT stage VI), suggesting a vigorous response of astrocytes to nearby Aβ plaques and NFTs that they ultimately cannot sustain and turn off as this exposure becomes chronic

Fig. 3 | Astrocyte transcriptomic changes along the stereotypical spatial progression of AD. a, Spatial trajectory gene sets resulting from clustering the $n = 504$ DEGs between any two adjacent nodes of the AD network from EC to V1. The y axis is the standardized gene expression, with gray lines representing individual genes, whereas the colored lines represent the mean trend. **b**, The first two vertical bars represent the association between the average expression of each spatial trajectory gene set in each donor and their pTau/tau ratio and Aβ plaque burden (red indicates statistically significant positive correlation; blue indicates statistically significant negative correlation; gray indicates NS). The last two vertical bars illustrate the results of an overlap test between each spatial trajectory gene set and the region-specific EC-high/EC-low and V1-high/V1-low gene sets derived from normal controls in Fig. 2 (red indicates statistically significant overlap with region-specific upregulated gene set; blue indicates statistically significant overlap with region-specific downregulated gene set; gray indicates NS). **c**, Functional characterization of each spatial trajectory gene set via pathway analysis; some relevant genes of each pathway are displayed on the right. ROS, reactive oxygen species.

https://doi.org/10.1038/s41593-024-01791-4

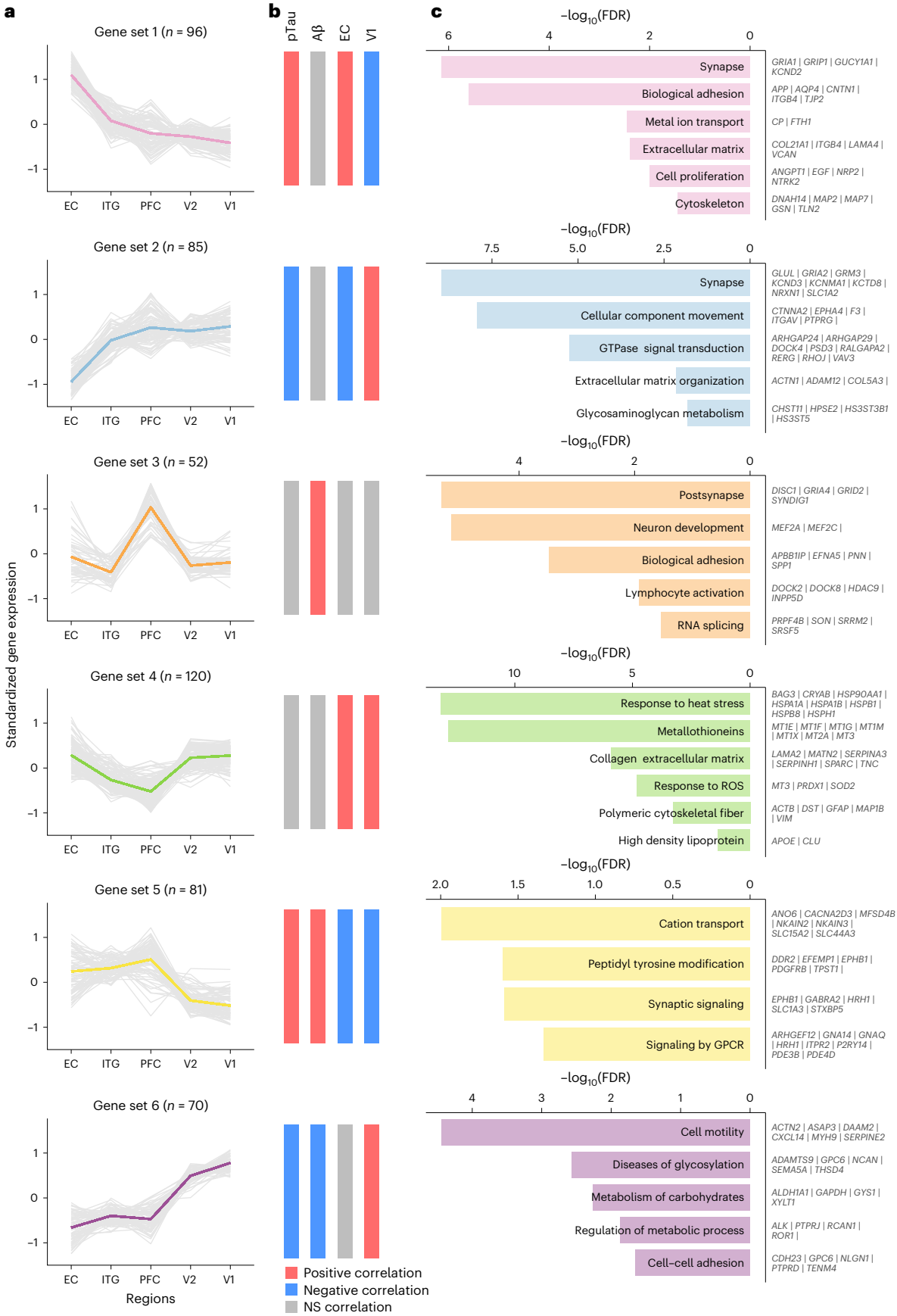

https://doi.org/10.1038/s41593-024-01791-4

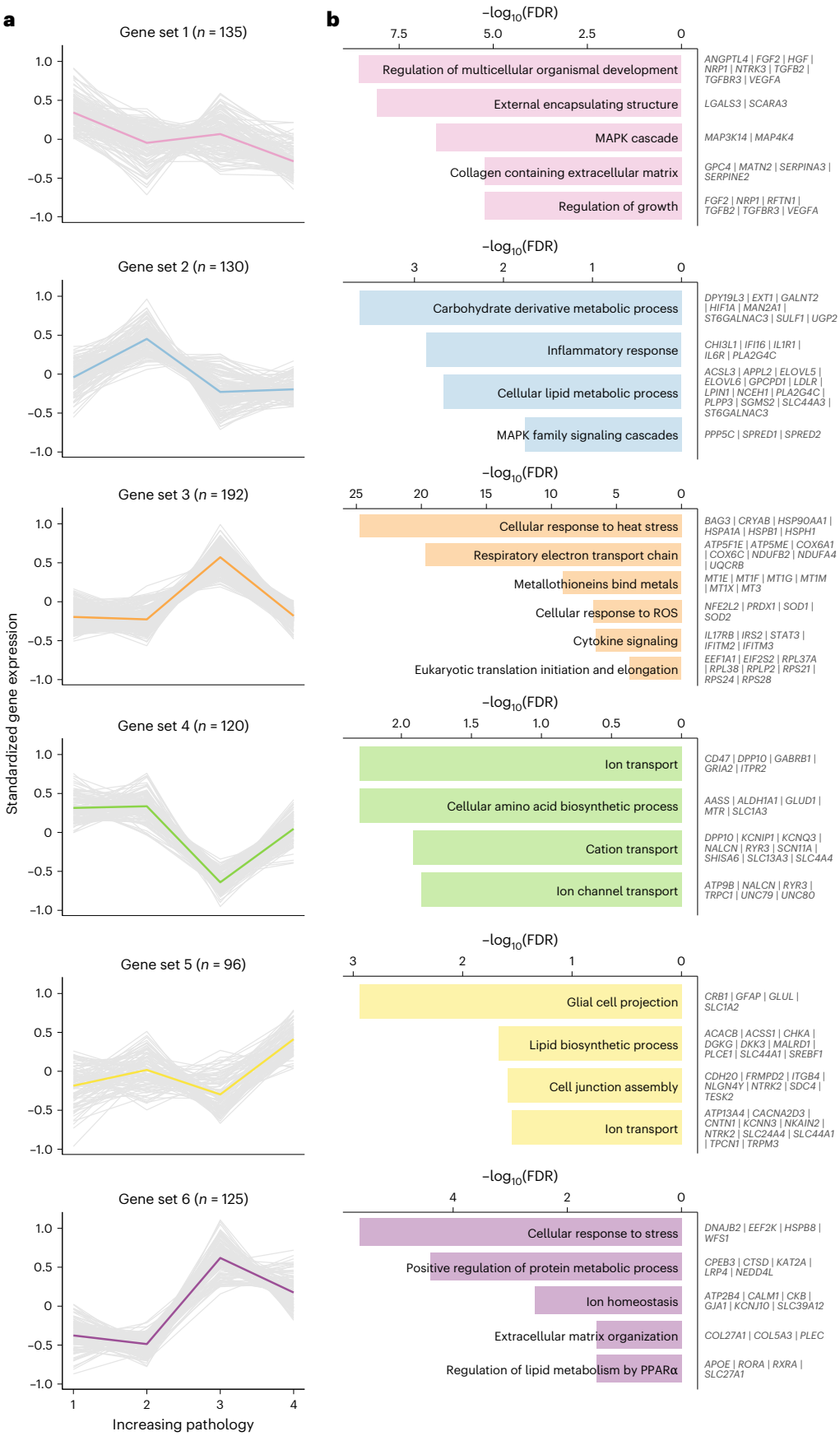

Fig. 4 | Astrocyte transcriptomic changes along the temporal progression of AD. a, Temporal trajectory gene sets resulting from clustering the $n = 798$ DEGs between any two adjacent pathology stages from early to end stage. The y axis is the standardized gene expression, with gray lines representing individual genes, whereas the colored lines represent the mean trend. **b**, Functional characterization of each temporal trajectory gene set via pathways analysis; some relevant genes of each pathway are displayed on the right. MAPK, mitogen-activated protein kinase; PPARα, peroxisome proliferator-activated receptor α.

(that is, response exhaustion). The upregulated late gene program comprised genes involved in proteostasis/response to heat stress (*AHSA1*, *BAG3*, *CCT4*, *CRYAB*, *DNAJA1*, *DNAJB1*, *DNAJB6*, *HSP90AA1*, *HSP90AB1*, *HSPA1A*, *HSPA1B*, *HSPA4*, *HSPA4L*, *HSPA8*, *HSPA9*, *HSPB1*, *HSPD1*, *HSPE1*, *HSPH1*, *MIB1*, *OTUD7B*, *SQSTM1*, *ST13*, *UBB*, *UBC*, *UBE2B* and *UBE2E2*), protein translation (*EEF1A1*, *EIF1*, *EIF2S2*, *RPL37A*, *RPL38*, *RPLP2*, *RPS21*, *RPS24* and *RPS28*), energy metabolism (*ENO1*, *GAPDH*, *LDHB* and *PGK1*), mitochondrial electron transport chain (*ATP5F1E*, *ATP5MD*, *ATP5ME*, *ATP5PF*, *COX6A1*, *COX6C*, *COX7C*, *NDUFA4*, *NDUFB2*, *NDUFB4*, *NDUFC1* and *UQCRB*), antioxidant defense (*NFE2L2*, *NXN*, *PRDX1*, *SOD1*, *SOD2* and the metallothionein genes (*MT1E*, *MT1F*, *MT1G*, *MT1M*, *MT1X* and *MT3*)), neuroinflammation including interferon response (*IFITM2*, *IFITM3*, *IL17RB*, *IRS2*, *NFAT5*, *PTGES3* and *STAT3*), cell–cell communication (*CD59*, *CDH23*, *CHL1*, *CNTNAP2*, *CNTNAP3*, *CNTNAP3B*, *FGFR1* and *RGMA*) and some genes involved in lipid metabolism (*ABHD3*, *CLU*, *OAZ1* and *OSBPL1A*), cytoskeleton (*CLIP2*, *MAP2*, *SYNM* and *VIM*), extracellular matrix (*MMP16*, *PLOD2*, *PLOD3*, *SERPINH1*, *SPP1* and *ST6GALNAC6*), synaptic function (*CAMK2D*, *CAMK2N1*, *FOS*, *GAB1*, *NRXN3* and *RIMS1*) and intracellular transport/trafficking (*ATP2C1*, *CPE*, *DYNLRB1*, *SLC7A5*, *SLC7A11*, *SLC9B2*, *SLC20A2* and *SNX3*). The downregulated late gene program included genes involved in glutamate neurotransmission (*GLUD1*, *GRIA2* and *SLC1A3*), extracellular matrix (*COL28A1*, *CSGALNACT1*, *EPM2A* and *GPC5*) and intracellular transport (*GOLGA8B*, *SLC4A4*, *SLC13A3* and *TVP23C*). Interestingly, many of these late-stage genes overlap with the Aβ/pTau-unrelated genes (gene set 4) of the spatial progression analysis. This lack of correlation with Aβ and pTau is likely explained by the apparent normalization of their expression levels in end-stage disease (Braak stage VI) despite the further accumulation of Aβ and especially pTau in all brain regions of Braak stage VI donors (Fig. 1d).

Moreover, we identified a smaller set (gene set 5) whose expression levels remained relatively stable throughout early, intermediate and late stages and only increased at the end stage (moderate/frequent NPs, Braak NFT stage VI). This gene set contained glutamate metabolism (*GLUL* and *SLC1A2*), extracellular matrix (*ADAMTSL3*, *COL21A1*, *HPSE2*, *SDC4* and *VCAN*), lipid metabolism (*ACACB*, *ACSS1*, *DGKG*, *OSBPL11*, *PHYHD1*, *PHYHIPL*, *PLCE1*, *PPARGC1A* and *SREBF1*), trophic factors (*FGFR3* and *NTRK2*), cell–cell communication (*CDH20*, *CLEC16A*, *CNTN1*, *ITGB4* and *NLGN4Y*) and intracellular transport (*DYNC2H1*, *SCLT1*, *SLC14A1*, *SLC18B1*, *SLC24A4* and *SLC44A1*) genes. Finally, gene set 6 had low expression at early and intermediate stages, peaked at the late stage and decreased at the end stage without returning to baseline; relevant genes pertained to proteostasis (*CTSD*, *DNAJB2*, *HSPB8* and *NEDD4L*), energy metabolism (*ALDH2*, *CKB* and *PFKP*), extracellular matrix (*B4GALNT4*, *COL5A3*, *COL27A1*, *CST3*, *FLRT2*, *PLEC* and *PLXNB1*), intracellular transport and trafficking (*ATP2B4*, *SLC27A1*, *SLC38A2*, *SLC39A11*, *SLC39A12* and *TRAK1*), cell–cell communication (*GJA1*), lipid metabolism (*APOE* and *LRP4*) and nuclear receptors (*RORA* and *RXRA*).

Compared to the spatial gene sets, the heatmap showing the differential expression of the individual genes comprising these temporal gene sets across pathology stages at the donor level showed slightly higher interdonor variability (Supplementary Fig. 4a), possibly reflecting differences in the duration of each stage across donors. Donor-level expression of representative genes for each temporal trajectory is shown in Supplementary Fig. 4b. Interestingly, there was minimal overlap between the spatial and temporal gene sets (Supplementary Fig. 4e), suggesting that a complex interplay of intrinsic properties of the regional microenvironment, local amounts of Aβ and pTau and duration of the exposure to Aβ and pTau insults governs astrocyte gene expression. Indeed, these results indicate that both brain region and Braak NFT stage should be carefully considered when comparing the astrocyte transcriptome of AD versus normal control brains because astrocyte transcriptomic responses to ADNC might be attenuated or exhausted in end-stage disease (Braak NFT stage VI) in severely and chronically affected brain areas.

Astrocyte clustering analysis reveals diverse transcriptomic programs across brain regions and pathology stages

While two broad categories of astrocytes, homeostatic and reactive, have been traditionally postulated, the above-mentioned results suggested a more complex picture of astrocyte reactivity, as put forward in a recent consensus statement on reactive astrocytes[1]. We asked whether distinct subpopulations or states can be distinguished based on their gene expression programs. To address this question, we randomly sampled 500 nuclei from each brain region of each donor and integrated and clustered these nuclei into nine distinct astrocyte subclusters (Uniform Manifold Approximation and Projection (UMAP) in Fig. 5a). Two small clusters had genes typically found in other cell types, specifically neurons (astNeu) and microglia (astMic), and were considered hybrids or doublets (although their estimated doublet score was very low). Inspection of both the top DEGs defining the subclusters (that is, subcluster marker genes available in Supplementary Data 6) and the enriched pathways revealed an interesting functional specialization of the remaining seven subclusters. The subcluster astH0 was enriched in glutamatergic (*GLUL*, *GRIA2*, *GRM3* and *SLC1A2*) and gabaergic (*SLC6A1* and *SLC6A11*) neurotransmission genes, along with potassium-buffering channels (*KCNJ10* and *KCNJ16*) and cell adhesion molecules involved in astrocyte–astrocyte (*GJA1*) and astrocyte–neuron interactions (*ERBB4* and *NRXN1*), consistent with a canonical protoplasmic homeostatic phenotype (Fig. 5b,c). By contrast, astR1 and astR2 were enriched in *GFAP*, *S100B*, HSF1-mediated stress response (*CRYAB*, *HSPA1B*, *HSPB8* and *UBC*), extracellular matrix (*CD44*, *COL21A1*, *GPC6*, *LAMA4*, *SERPINA3*, *TNC* and *VCAN*) and oxidative stress (*MAOB*), but differed in some other marker genes (for example, *ADAMTSL3*, *AQP1*, *C3*, *MAP1B*, *MAPT* and *SOD2* in astR1 versus *GRIA1* and *SPARC* in astR2), suggesting that they are different states of astrocyte reactivity (Fig. 5b,c). Subcluster astR0 also exhibited a reactive phenotype and was further enriched in extracellular

Fig. 5 | Clustering reveals homeostatic, reactive and intermediate astrocytes. **a**, UMAP plot of a subsample of 500 astrocyte nuclei from each donor and region, with the colors representing each of the ten astrocyte subclusters resulting from the clustering. **b**, Bubble plots illustrate the expression *z* scores of selected marker genes defining the nine astrocyte subclusters. **c**, Characterization of astrocyte subclusters with pathway enrichment analysis. Bar plots represent the statistical significance ($-\log_{10}$(FDR)) of the functional pathways defining the main astrocyte subclusters. **d**, Double fluorescence immunohistochemistry for selected markers with thioflavin-S (ThioS) counterstaining in FFPE sections from the temporal association cortex of control (CTRL) and AD donors show reduced expression of some homeostatic markers and increased expression of some reactive markers in GFAP$^+$ astrocytes surrounding some ThioS$^+$ Aβ plaques. Note that representative photomicrographs from at least three CTRL and three AD donors were taken with similar exposure time and display settings for appropriate comparison. Scale bar = 10 µm. **e**, Violin plots show a statistically significant or marginally significant higher expression of reactive astrocyte markers in AD (pathology groups 3 and 4, $n = 7$) versus CTRL (pathology group 1, $n = 6$) centered within and around ThioS$^+$ Aβ plaques. Individual data points are shown as dots, and horizontal lines represent the median value. Note that the gradient of expression of these reactive astrocyte markers from ThioS$^+$ Aβ plaques to the plaque vicinity (≤50 µm) and to plaque-free distant areas (>50 µm from nearest plaque edge) in the AD temporal neocortex, while no such gradient is observed relative to sham plaques from CTRL cortex. Data from AD donors correspond to $n = 50$ randomly selected ThioS$^+$ Aβ plaques per donor distributed throughout all layers of a temporal neocortex tissue section, their 50 µm halo and $n = 50$ distant (>50 µm) ROIs of similar size per donor. For CTRL donors, $n = 50$ sham plaques of similar size per donor, their 50 µm halo and $n = 50$ ROIs of similar size located far from them (>50 µm) per donor were analyzed. Data were analyzed running mixed-effects models with diagnosis and location as fixed effects and donor ID as random effect to account for within-donor correlation. FGFR, fibroblast growth factor receptor.

https://doi.org/10.1038/s41593-024-01791-4

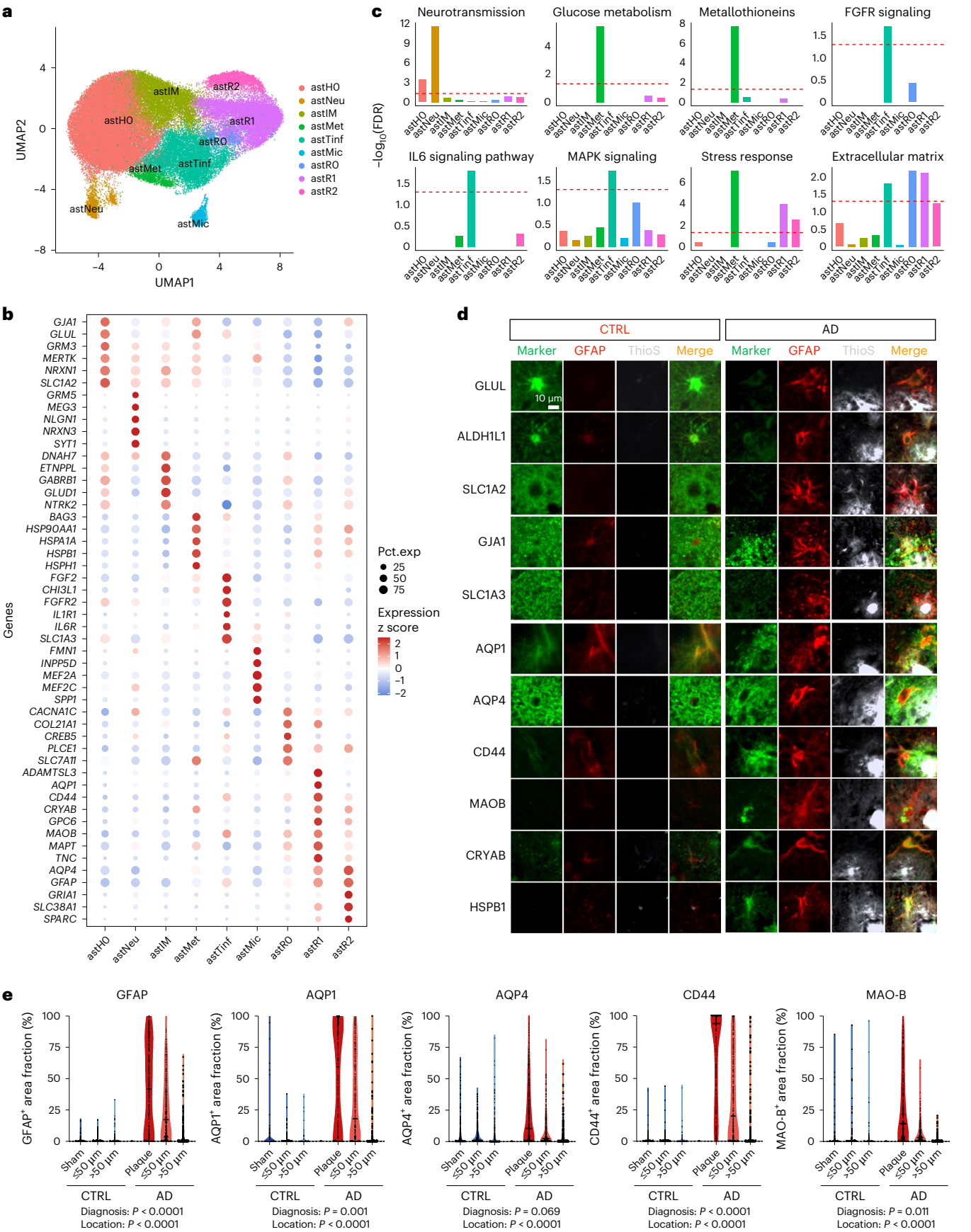

matrix genes (*COL21A1*, *COL24A1*, *COLGAT* and *LAMA2*). Fluorescence immunohistochemistry validated some of these homeostatic and reactive markers in postmortem brain sections from control and AD donors, and a spatial quantitative analysis centered in thioflavin-S-positive dense-core Aβ plaques demonstrated a gradient of expression of the reactive markers from the plaque to the peri-plaque halo (≤50 µm) to areas distant (>50 µm) from plaques in the AD cortex, whereas no effect of sham plaques was observed in control cortex (Fig. 5d,e and Supplementary Figs. 5–7). Fluorescence in situ hybridization via RNAScope confirmed the expression of *MAPT* by astrocytes (Supplementary Fig. 8).

The subcluster of intermediate astrocytes (astIM) had somewhat overlapping profiles between homeostatic and reactive and expressed classic homeostatic genes, although at lower levels than astH0, but also higher levels of certain genes (*DNAH7*, *ETNNPL*, *GABRB1*, *GLUD1* and *NTRK2*; Fig. 5b,c). Subcluster astMet was characterized by glucose metabolism (*ENO1*, *ENO2*, *GAPDH*, *GYS1*, *HK1*, *HK2*, *LDHA*, *PDK1*, *PDK3*, *PGK1*, *PFKP* and *PKM*) and metallothioneins (*MT1E*, *MT1F*, *MT1G*, *MT1M*, *MT1X*, *MT2A* and *MT3*) but also exhibited a stress response (*BAG3*, *HSP90AA1*, *HSPA1A*, *HSPB1* and *HSPH1*). Another subcluster, which we named astTinf, was enriched in growth factors (*FGF1*, *FGF2*, *FGFR2*, *HGF* and *OSMR*) and interleukin signaling (*CHI3L1*, *IL1R1*, *IL6R*, *ITGB1*, *MAPK4* and *SOCS3*) besides extracellular matrix.

Taken together, these data indicate that there are subclusters of astrocytes with markedly distinct transcriptomic programs from the classic homeostatic and reactive states.

Dynamic transcriptomic changes in astrocyte subclusters along AD progression

Finally, we asked whether the above-mentioned astrocyte subclusters represent stable astrocyte subpopulations or, conversely, dynamic states responsive to AD neuropathology. Toward that end, we first examined changes in subcluster frequency and cell density along the spatial and temporal axes of AD progression (Fig. 6a,b and Supplementary Fig. 9a). Notably, the proportion of homeostatic astH0 astrocytes was significantly reduced in EC versus all other regions but did not change with pathology stages, whereas both astR1 and astR2 reactive astrocytes were more frequent in EC and ITG, and the frequency of astR1 tended to increase with pathology stages. The proportion of reactive astR0 astrocytes increased in parallel with pathology stages and decreased along brain regions from EC to V1. Similarly, the frequency of astIM declined along the spatial axis but was reduced only in pathology stage 3. In contrast, the frequency of subclusters astMet and astTinf remained stable across the five brain regions but behaved differently along the four pathology stages. astMet was increased specifically in pathology stage 3, whereas astTinf declined along pathology stages. While some of the subclusters were associated with age, the effect sizes were very small ($\beta = -0.008$ to 0.004). Also, only astMet was significantly associated with sex (higher frequency in female donors, $P < 0.005$), but the effect size was small ($\beta = 0.046$).

Next, we compared the marker genes of the astrocyte subclusters with the spatial and temporal gene sets identified in the previous sections and asked whether the spatial and temporal gene sets were overrepresented or underrepresented in any subcluster (Supplementary Fig. 9b,c). As expected, the homeostatic astH0 and reactive astR0, astR1 and astR2 subclusters were enriched in spatial gene sets that correlated with the pTau/tau ratio. Specifically, the reactive subclusters had a positive enrichment score for spatial gene set 1 (positively correlated with pTau) as well as spatial gene set 4 (stress chaperones/heat-shock response genes) and a negative enrichment score for spatial gene set 2 (negatively correlated with pTau), whereas the homeostatic subcluster astH0 demonstrated the opposite effects (Supplementary Fig. 9b). The astIM subcluster was also enriched in the pTau/tau-associated spatial gene set 1.

While the homeostatic and reactive subclusters were enriched in the spatial gene sets, the astMet and astTinf subclusters were enriched in several temporal gene sets (Supplementary Fig. 9c). Of note, astTinf exhibited a positive enrichment of temporal gene sets 1, 2 and 3, corresponding to early, intermediate and late astrocyte gene programs, but its frequency significantly decreased along pathology stages (Fig. 6b). In contrast, astMet exhibited a positive enrichment in temporal gene set 3 (characterized by upregulation of proteostasis, mitochondrial electron transport chain and metallothioneins in pathology stage 3 and normalization in pathology stage 4) and a negative enrichment of temporal gene set 4 (characterized by downregulation of ion transport in pathology stage 3 and normalization in pathology stage 4), suggesting that astMet are the exhausted astrocytes. This is consistent with the significantly increased frequency of astMet in pathology stage 3 relative to pathology stages 1 and 2, with a subsequent decrease in pathology stage 4 (Fig. 6b). Notably, AstMet was not enriched in senescence genes[34] ($P \geq 0.4$), suggesting that exhausted astrocytes are not senescent. Together, these data suggest that astMet are undergoing exhaustion, that is, failure in proteostasis and energy metabolism, after prolonged exposure to ADNC (Braak stage VI). Fluorescence in situ hybridization in the V2 region via RNAScope for *ALDH1L1* (to label all astrocytes) and *HSPB1* (a representative gene of temporal gene set 3 encoding the small chaperone HSP27) confirmed the highest expression in stage 3 and very low expression in stage 4 (Supplementary Fig. 10).

Furthermore, to understand the dynamics of the transitions across the astrocyte subclusters, we used pseudotime analysis—a computational technique that orders cells along a continuous trajectory based on their gene expression profile. Initiating from astH0 as the origin, pseudotime analysis revealed a sequential pattern of gene expression changes progressing to astR0, astR1 and astR2 reactive astrocytes primarily through astIM (Fig. 6c). To analyze the cell transition probabilities, we used CellRank[35], which leverages splicing dynamics to determine the ratio between spliced and unspliced products as a proxy for expression dynamics (stable, induction or repression). This cell transition analysis confirmed a transition from astH0 to astR1 through astIM (Fig. 6d). Interestingly, the homeostatic astH0 astrocytes also transitioned to astMet and astTinf, which appeared to be terminal states with no further progression into the reactive subclusters (Fig. 6d). Heatmaps of marker genes illustrating the transitions of homeostatic astH0 astrocytes further supported the finding that astIM is an intermediate state between homeostatic and reactive astrocytes, whereas astMet and astTinf are distinct subclusters that deviate from the prototypical homeostatic-to-reactive transition path (Fig. 6e).

These findings indicate that astMet and astTinf are unique terminal subclusters with a complex, stage-dependent response to ADNC, suggesting that their response is driven by the cumulative effect of such toxic exposures over time.

Comparison with other human snRNA-seq datasets

Furthermore, we asked whether the astTinf and exhausted astMet astrocytes are unique to our dataset or whether they might also be

Fig. 6 | Dynamics of astrocyte transcriptomic changes. a, Proportion of astrocyte subclusters across brain regions ($n = 22$ EC, $n = 31$ ITG, $n = 28$ PFC, $n = 31$ V2 and $n = 32$ V1). **b**, Proportion of astrocyte subclusters across pathology stages ($n = 30$ stage 1, $n = 39$ stage 2, $n = 36$ stage 3 and $n = 39$ stage 4). In both **a** and **b**, each dot represents a unique sample (individual + region). Horizontal line in each box represents the median value; boxes extend from the 25th to the 75th percentile of values in each group; whiskers extend from the 5th to the 95th percentile. **c**, Pseudotime (transcriptomics distance from the origin) is visualized on the UMAP plot with the homeostatic astH0 subcluster as the origin. **d**, Velocity streams calculated with CellRank on our subsampled astrocytes. **e**, Heatmap showing the top transitional genes along the pseudotime, with astH (blue) and astR (red) marker genes labeled to the right of the heatmap. Individual cells from subclusters and pseudotime are shown on the top annotation bar.

https://doi.org/10.1038/s41593-024-01791-4

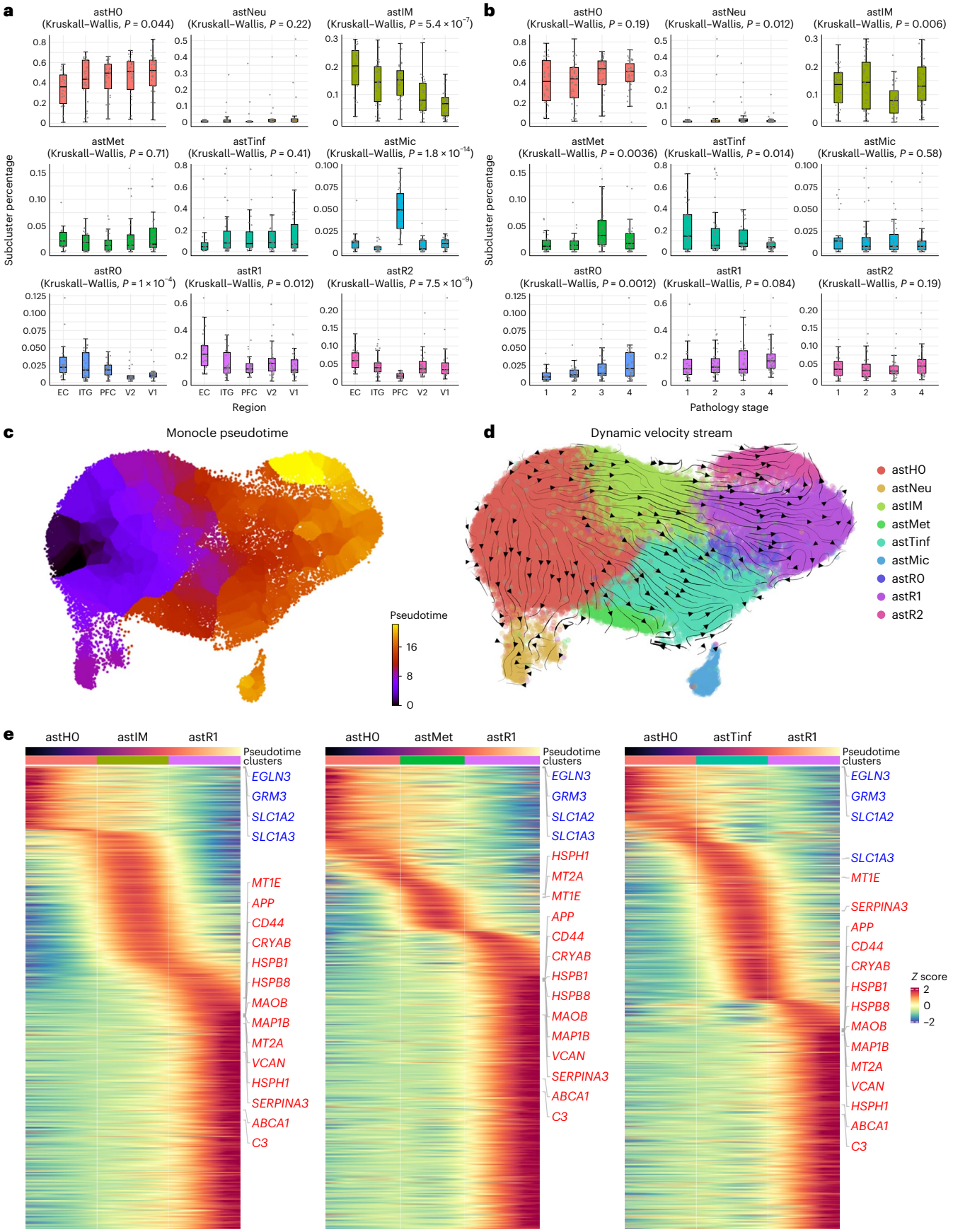

detectable in other human brain AD snRNA-seq datasets. To address this question, we used the Seurat anchor integration tool for label transfer to project astrocytes from nine previously published datasets[9–17] (Supplementary Data 7) onto ours based on the similarity of transcriptomic profile. The earlier datasets[9,10,13] had fewer total numbers of astrocytes relative to the most recent studies[14,17] and the vast majority mapped as homeostatic astH0 or reactive astR0, astR1 and astR2 astrocytes (Fig. 7a). All the studies had some representation of the entire continuum of changes observed in our AD progression study. Although all but one study[10] had astTinf, only the largest study—the Seattle Alzheimer's Disease Brain Cell Atlas (SEA-AD)[17], performed in the middle temporal gyrus—had a sizable representation of the exhausted astMet subcluster. We next compared the frequency of astTinf and astMet along disease stages and found a similar trend toward decreasing astTinf frequency with pathology stages in SEA-AD. However, there was no significant change in astMet frequency across Braak stages in these nine datasets, suggesting that the exhaustion phenomenon revealed by astMet is unique to our dataset (Fig. 7b). Finally, we also compared the marker genes of the astrocyte subclusters reported in the nine previous studies with ours (see Supplementary Data 7 for details on which gene sets were chosen from the studies). While our homeostatic and reactive subcluster marker genes overlapped substantially with those from previous studies, astTinf and astMet appeared to be unique to our study (Fig. 7c), suggesting that our sampling scheme across brain regions and pathology stages was key for the identification of these subclusters.

Together, these results underscore the dynamic, complex and nonlinear pattern of astrocyte transcriptomic changes along AD progression, uncovering two terminal states that are off-pathway the prototypical astrocyte reactivity, including a previously unrecognized exhausted state. Additionally, they highlight the importance of examining the full spectrum of ADNC severity, including intermediate phenotypes and multiple hierarchically affected brain regions.

AD progression atlas

To facilitate access to our rich dataset of AD progression, we have developed a web-based tool for query and visualization (https://ad-progression-atlas.partners.org). The tool allows gene expression queries at the sample level by various parameters (such as Braak NFT stage, CERAD NP score, Aβ plaque load and pTau/tau ratio). It also enables cell-level queries and displays results as feature, proportion or bubble plots.

Discussion

We generated a large snRNA-seq dataset of human astrocytes across five brain regions, encompassing the normal aging to severe AD continuum. The analysis of this large dataset provided important clues on the regional heterogeneity of astrocyte transcriptome in the normal aging brain and the transcriptomic programs that astrocytes activate and deactivate in the AD brain in response to the stereotypical spatiotemporal progression of ADNC.

First, we observed significant regional differences in astrocyte transcriptome in the brains from normal controls, with EC and V1 regions showing the highest numbers of upregulated and downregulated DEGs. The EC, specifically layer II, is the first region affected by NFTs and neurodegeneration in most AD cases[20,36]. Here we identified an EC-specific astrocyte signature, which included changes in genes relevant to AD pathophysiology such as an upregulation of *APP* and *APOE* and a downregulation of *SLC1A2* (encoding the glutamate transporter EAAT2, a.k.a. GLT-1) and *MAPT* (encoding the microtubule-associated protein tau) relative to other cortical regions. Noteworthy, an increase in *SLC1A2* expression in EC astrocytes has been associated with resilience to AD pathology[37], and downregulation of *SLC1A2* is predicted to increase the excitability of glutamatergic neurons[38], suggesting a potential role of astrocytic genes in EC vulnerability to AD. Notably, we unexpectedly found robust expression of *RORB* in astrocytes, although *RORB* had previously been identified by snRNA-seq as a marker gene for excitatory EC neurons that are vulnerable to NFTs and neurodegeneration in AD[12]. By contrast, our study identified *RORB* as one of the downregulated genes in EC astrocytes, arguing for future investigation into its cell type-specific functions. The virtual absence of Aβ deposits across brain regions in these control donors enabled us to isolate the effects of pTau pathology on the astrocyte transcriptome and to confirm that the EC signature cannot be explained just by the NFTs already present in the EC in donors with Braak NFT stages I and II. On the other hand, the V1 signature in control donors could be, at least partly, mediated by the astrocytes from the stria of Gennari or Vicq-d'Azyr's band, a strip of white matter that lies between layers IVb and IVc of the calcarine cortex and defines the striate cortex of BA17 (ref. 39), because white matter fibrous astrocytes are markedly different from protoplasmic cortical astrocytes[40,41]. Thus, the substantial regional heterogeneity found in the normal aging brain warrants careful interpretation of single-region studies comparing AD versus control donors.

Second, we leveraged our multiregion sampling of many donors with various levels of ADNC to investigate associations between astrocyte gene expression levels and the spatiotemporal progression typical of AD. When we rank ordered the five brain regions along a spatial axis following the typical hierarchical progression of AD and compared the astrocyte transcriptome from all donors across any two adjacent nodes of the AD network, we were able to identify multiple gene sets following distinct spatial trajectories. We found that these various spatial trajectories of astrocyte gene expression could only be partly explained by the regional differences detected in the normal controls with virtually no Aβ plaques and pTau pathology mostly restricted to the EC. On the contrary, except for one gene set, all other spatial trajectories were also associated with the local levels of either Aβ, pTau or both, enabling us to investigate Aβ- and pTau-associated gene signatures. Aβ and pTau levels positively correlated with different synapse-associated, cell–cell communication and cytoskeletal genes. Of note are astrocyte genes involved in synaptic function that are dysregulated in parallel to the stereotypical march of pTau pathology across cortical association areas. Furthermore, the negative correlation between the *SLC1A2*-containing,

Fig. 7 | Comparison with publicly available human AD snRNA-seq datasets. **a**, UMAP plot of astrocytes from the present study and nine other previously published studies after anchor-based integration onto data in the present study. **b**, Boxplots showing the frequency of astMet (left) and astTinf (right) in all studies. Exhaustion phenomenon was only observed in the present study. Horizontal line in each box represents the median value; boxes extend from the 25th to the 75th percentile of values in each group; whiskers extend from the 5th to the 95th percentile. Each dot represents one unique sample (individual + region). Present study—$n = 30$ Braak stages 0–II, $n = 39$ Braak stages III–IV, $n = 36$ Braak stage V and $n = 39$ Braak stage VI in; ref. 9—$n = 24$ no-pathology, $n = 15$ early pathology and $n = 9$ late-pathology; ref. 10—$n = 6$ control and $n = 6$ AD; ref. 13—$n = 9$ control and $n = 12$ AD; ref. 11—$n = 11$ control, $n = 11$ AD (TREM2-CV) and $n = 10$ AD (TREM2-R62H); ref. 12—$n = 14$ Braak stages 0–II and $n = 6$ Braak stage VI; ref. 15—$n = 13$ control and $n = 11$ AD; ref. 14—$n = 7$ control and $n = 10$ AD; ref. 16—$n = 4$ control and $n = 11$ AD; SEA-AD study—$n = 12$ Braak stages 0–II, $n = 57$ Braak stages III–IV, $n = 67$ Braak stage V and $n = 28$ Braak stage VI. Significance was evaluated by a two-sided Welch's t test. P values were adjusted using the Benjamini–Hochberg method to correct for multiple comparisons when two or more comparisons were conducted within studies. Left, in the present study, Braak stages 0–II versus Braak stage V (**$P = 0.0015$), Braak stages III–IV versus Braak V (**$P = 0.0015$) and Braak stage V versus Braak stage VI (*$P = 0.018$). Right, in the present study, Braak stages 0–II versus Braak stage VI (***$P = 5 \times 10^{-4}$), Braak stages III–IV versus Braak stage VI (**$P = 0.003$) and Braak stage V versus Braak stage VI (***$P = 8 \times 10^{-4}$). In ref. 11, control versus AD (TREM2-CV) **$P = 0.008$, control versus AD (TREM2-R62H) **$P = 0.008$. **c**, Heatmap showing the overlap of the astrocyte subcluster marker genes with gene sets from the other studies.

https://doi.org/10.1038/s41593-024-01791-4

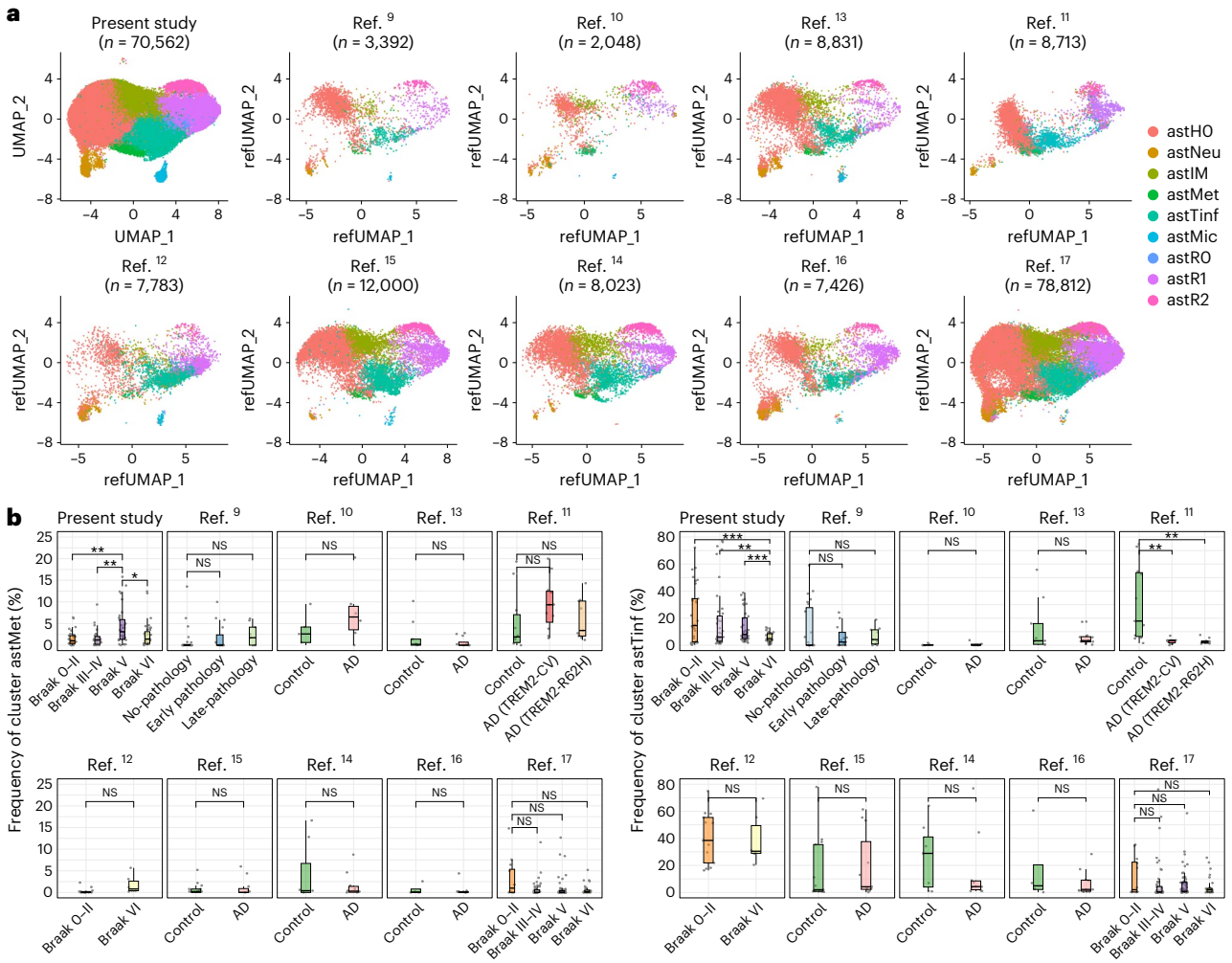

synapse-associated spatial gene set and pTau levels is consistent with the reported association between a PET-based tau-spreading network and a gradient of expression of glutamatergic synaptic genes, singularly *SLC1A2* (ref. 42). Thus, these results could be indicating that astrocytes, as part of the tripartite excitatory synapses, have a key role in synaptic dysfunction and the *trans*-synaptic propagation of pTau between excitatory neurons along vulnerable AD neural networks. On the other hand, genes correlated with both Aβ and pTau levels (a.k.a. pan-reactive) consisted of an upregulation of GPCR-mediated signaling and intracellular trafficking and a downregulation of energy metabolism, further suggesting a synergistic effect of Aβ and pTau on the astrocyte transcriptome[5]. The latter result also suggests that astrocytes undergo an energy failure as a result of chronic exposure to both Aβ and pTau. Notably, previous bulk transcriptomic analyses have highlighted energy metabolism deficits as a feature of AD and other neurodegenerative diseases[43,44], but have either attributed this finding to the severe neuronal dysfunction and loss or imputed it to astrocytes only through indirect computational methods[1]. Our data confirm that astrocytes, in addition to neurons, suffer mitochondrial dysfunction and energy deficits that contribute to these observed bulk RNA changes and could also potentially contribute to clinical progression. Intriguingly, astrocytes have been reported to contribute to the (^{18}F)fluoro-deoxy-glucose (FDG)–positron emission tomography (PET) signal via the glutamate transporter EAAT2/GLT-1, encoded by *SLC1A2* (ref. 45), whose expression is negatively associated with pTau. Also interestingly, higher plasma GFAP levels have been associated with higher (^{18}F)FDG–PET signals in early AD[46]. Thus, reactive astrocytes may initially increase their metabolic rate but finally fail to meet their energy needs and contribute to the typical bilateral temporoparietal hypometabolism observed in AD. On the other hand, another sizable gene set (gene set 4, $n = 120$), characterized by its lack of correlation with either Aβ or pTau levels and highest expression levels in the EC and V1, was composed of genes related to the cytoskeleton (including *GFAP*), lipid metabolism (including *APOE* and *CLU*), calcium homeostasis, extracellular matrix, heat-shock proteins and antioxidant defense (for example, metallothioneins), suggesting a nonlinear heterogeneous response to ADNC in the different cortical regions.

We also examined the astrocyte transcriptomic changes along the temporal axis by analyzing the effect of increasing ADNC severity, which matched well with increasing local levels of Aβ and pTau in each brain region. Assuming that autopsy findings of ADNC severity can be temporally ordered, which is well supported by the PET imaging biomarker literature, this analytical approach revealed what appears to be successive waves of astrocyte transcriptomic programs in intermediate versus late versus end-stage disease. At the intermediate ADNC stage, astrocytes induced trophic and survival factors (significantly the *HIF1A* gene, encoding the hypoxia-inducible factor 1α (HIF1α), which has been shown to be a major driver of energy metabolism changes in AD reactive microglia[47]), extracellular matrix (for example, *GPC6* and *TNC*), cytoskeleton and neuroinflammation (notably *CHI3L1*, encoding for the fluid biomarker of reactive astrogliosis YKL-40 (ref. 48) and the endogenous inhibitor of calcineurin *RCAN1*) genes different from those predominant in the earliest ADNC stage. Additionally, lipid metabolism (notably the APOE receptor *LDLR*[49] and the fatty acid elongases *ELOVL5* and *ELOVL6*, which could result in the generation of purportedly toxic saturated long-chain fatty acids[50]), glycosaminoglycan metabolism and synapse-associated and GPCR-mediated signaling genes were also upregulated in the intermediate stage. We separated Braak stages V and VI donors to test the hypothesis that gene expression by reactive astrocytes may be impacted by chronic exposure to Aβ and pTau, represented by the latter end stage. Indeed, the distinguishing feature between Braak NFT stages V and VI is not just the presence of NFTs in the primary visual (V1), motor and sensory cortical areas, but more severe neurofibrillary degeneration[21] and atrophy throughout the cortical mantle[51]. We observed that at the late stage (Braak stage V), the astrocyte transcriptomic response was dominated by upregulation of genes related to protein translation (that is, elongation factors and ribosomal subunits), proteostasis (that is, many small chaperones and heat-shock proteins), energy metabolism (for example, *GAPDH* and *LDHB*), mitochondria electron transport chain, neuroinflammation (notably interferon response genes and *STAT3*), antioxidant defense (for example, *SOD1*, *SOD2* and many metallothionein genes) and the cytoskeleton (for example, *SYNM* and *VIM*), suggesting a full-blown, all-hands-on-deck adaptive response to nearby pervasive and conspicuous ADNC. Surprisingly, we observed that many of the genes upregulated during late stage (Braak stage V) decreased or even returned to baseline during end-stage disease (Braak stage VI), including those involved in proteostasis (for example, heat-shock response), energy metabolism and mitochondrial oxidative phosphorylation, lipid metabolism (significantly *APOE* and *CLU*), cytoskeleton and extracellular matrix, suggesting an exhaustion of astrocyte response. Many of the genes blunted in the end stage overlapped with the Aβ/pTau-uncorrelated genes (gene set 4) found in the spatial progression analysis, thereby explaining their lack of correlation with Aβ and pTau levels. We note that this exhausted phase of astrocyte response in Braak stage VI donors has not been previously described and may have confounded previous studies that compared only control and severe AD donors or grouped late- and end-stage donors (Braak stage V/VI) together[9–15].

Taken together, these findings reinforce the idea that AD-associated reactive astrogliosis tracks with the spatiotemporal progression of AD, highlighting a severe end-stage dysfunctional or maladaptive response of astrocytes likely caused by their chronic exposure to Aβ, pTau and ongoing neurodegeneration[52].

Third, we identified distinct subclusters of homeostatic and reactive astrocytes based on their gene expression profiles. We found that homeostatic astrocytes constitute the majority of the astrocyte population, regardless of the severity of AD pathology, and express higher levels of typical homeostatic genes such as glutamate metabolism-related genes, whereas reactive astrocytes represent less than 25% of all astrocyte nuclei and express higher levels of aquaporins, heat-shock proteins, extracellular matrix and cytoskeletal genes. Of note, many of these upregulated gene products have been demonstrated in AD reactive astrocytes via immunohistochemistry, especially near dense-core, typically neuritic, Aβ plaques[53]. Notably, we found a subcluster of astIM that represents a transitional state between homeostatic and reactive astrocytes, arguing against the latter being separate astrocyte subpopulations. The following lines of evidence support this interpretation: (1) the transcriptomic profile of astIM had overlapping characteristics between homeostatic (astH0) and reactive (astR0/R1/R2), (2) the frequency of the astIM subcluster declined along AD pathology stages and (3) astIM astrocytes were transcriptionally the most dynamic based on both pseudotime and cell transition/RNA velocity analyses.

These results are consistent with a dynamic phenotypic change of astrocytes from homeostatic to reactive through an intermediate state in response to their microenvironment conditions, namely the presence of Aβ plaques and NFTs[23,54–57], and ongoing work will define the molecular actors involved in these transitions in AD[58].

Besides the astH0-to-astIM-to-astR prototypical transition, cell transition analysis revealed two distinct routes of transition from astH0 to other terminal astrocytic states (astTinf and astMet). AstTinf is characterized by a strong trophic factor response mainly mediated by fibroblast growth factor receptor (FGFR) and transforming growth factor β receptor (TGFR) as well as heat-shock stress and inflammation genes. AstMet is enriched in glucose metabolism, metallothioneins and extracellular matrix genes and corresponds to the exhausted astrocytes whose proportion and gene expression program peak in AD late stage (Braak stage V) and normalize in end stage (Braak stage VI).

In summary, our five-region snRNA-seq study of astrocytes from 32 donors spanning the normal aging-severe AD continuum provides evidence of the regional diversity of astrocytes in the normal aging brain, demonstrates the complexity of their transcriptomic responses upon chronic exposure to ADNC, suggests Aβ plaque- and pTau-associated unique signatures of astrocytic reactions and uncovers the existence of intermediate states that appear to be transitional between homeostatic and reactive astrocytes. Overall, our findings highlight critical functional alterations of astrocytes—including proteostasis and metabolic—that suggest a complex trajectory of astrocyte from an adaptive response to a maladaptive dysfunction contributing to AD progression.

Online content

Any methods, additional references, Nature Portfolio reporting summaries, source data, extended data, supplementary information, acknowledgements, peer review information; details of author contributions and competing interests; and statements of data and code availability are available at https://doi.org/10.1038/s41593-024-01791-4.

References

1. Escartin, C. et al. Reactive astrocyte nomenclature, definitions, and future directions. *Nat. Neurosci.* **24**, 312–325 (2021).
2. Verkhratsky, A. & Nedergaard, M. Physiology of astroglia. *Physiol. Rev.* **98**, 239–389 (2018).
3. Orre, M. et al. Isolation of glia from Alzheimer's mice reveals inflammation and dysfunction. *Neurobiol. Aging* **35**, 2746–2760 (2014).
4. Srinivasan, K. et al. Untangling the brain's neuroinflammatory and neurodegenerative transcriptional responses. *Nat. Commun.* **7**, 11295 (2016).
5. Jiwaji, Z. et al. Reactive astrocytes acquire neuroprotective as well as deleterious signatures in response to Tau and Aβ pathology. *Nat. Commun.* **13**, 135 (2022).
6. Habib, N. et al. Disease-associated astrocytes in Alzheimer's disease and aging. *Nat. Neurosci.* **23**, 701–706 (2020).
7. Wu, T. et al. Complement C3 is activated in human AD brain and is required for neurodegeneration in mouse models of amyloidosis and tauopathy. *Cell Rep.* **28**, 2111–2123 (2019).
8. Endo, F. et al. Molecular basis of astrocyte diversity and morphology across the CNS in health and disease. *Science* **378**, eadc9020 (2022).
9. Mathys, H. et al. Single-cell transcriptomic analysis of Alzheimer's disease. *Nature* **570**, 332–337 (2019).
10. Grubman, A. et al. A single-cell atlas of entorhinal cortex from individuals with Alzheimer's disease reveals cell-type-specific gene expression regulation. *Nat. Neurosci.* **22**, 2087–2097 (2019).
11. Zhou, Y. et al. Human and mouse single-nucleus transcriptomics reveal TREM2-dependent and TREM2-independent cellular responses in Alzheimer's disease. *Nat. Med.* **26**, 131–142 (2020).
12. Leng, K. et al. Molecular characterization of selectively vulnerable neurons in Alzheimer's disease. *Nat. Neurosci.* **24**, 276–287 (2021).
13. Lau, S. F., Cao, H., Fu, A. K. Y. & Ip, N. Y. Single-nucleus transcriptome analysis reveals dysregulation of angiogenic endothelial cells and neuroprotective glia in Alzheimer's disease. *Proc. Natl Acad. Sci. USA* **117**, 25800–25809 (2020).
14. Sadick, J. S. et al. Astrocytes and oligodendrocytes undergo subtype-specific transcriptional changes in Alzheimer's disease. *Neuron* **110**, 1788–1805 (2022).
15. Smith, A. M. et al. Diverse human astrocyte and microglial transcriptional responses to Alzheimer's pathology. *Acta Neuropathol.* **143**, 75–91 (2022).
16. Dai, D. L., Li, M. & Lee, E. B. Human Alzheimer's disease reactive astrocytes exhibit a loss of homeostastic gene expression. *Acta Neuropathol. Commun.* **11**, 127 (2023).
17. Gabitto, M. I. et al. Integrated multimodal cell atlas of Alzheimeras disease. *Nat. Neuro.* https://doi.org/10.1038/s41593-024-01774-5 (2024).
18. Gerrits, E. et al. Distinct amyloid-β and tau-associated microglia profiles in Alzheimer's disease. *Acta Neuropathol.* **141**, 681–696 (2021).
19. Bryant, A. et al. Endothelial cells are heterogeneous in different brain regions and are dramatically altered in Alzheimer's disease. *J. Neurosci.* **43**, 4541–4557 (2023).
20. Braak, H. & Braak, E. Neuropathological staging of Alzheimer-related changes. *Acta Neuropathol.* **82**, 239–259 (1991).
21. Braak, H., Alafuzoff, I., Arzberger, T., Kretzschmar, H. & Del Tredici, K. Staging of Alzheimer disease-associated neurofibrillary pathology using paraffin sections and immunocytochemistry. *Acta Neuropathol.* **112**, 389–404 (2006).
22. McKenzie, A. T. et al. Brain cell type specific gene expression and co-expression network architectures. *Sci. Rep.* **8**, 8868 (2018).
23. Serrano-Pozo, A. et al. Reactive glia not only associates with plaques but also parallels tangles in Alzheimer's disease. *Am. J. Pathol.* **179**, 1373–1384 (2011).
24. Perez-Nievas, B. G. & Serrano-Pozo, A. Deciphering the astrocyte reaction in Alzheimer's disease. *Front Aging Neurosci.* **10**, 114 (2018).
25. Morel, L. et al. Molecular and functional properties of regional astrocytes in the adult brain. *J. Neurosci.* **37**, 8706–8717 (2017).
26. John Lin, C. C. et al. Identification of diverse astrocyte populations and their malignant analogs. *Nat. Neurosci.* **20**, 396–405 (2017).
27. Chai, H. et al. Neural circuit-specialized astrocytes: transcriptomic, proteomic, morphological, and functional evidence. *Neuron* **95**, 531–549 (2017).
28. Clarke, L. E. et al. Normal aging induces A1-like astrocyte reactivity. *Proc. Natl Acad. Sci. USA* **115**, E1896–E1905 (2018).
29. Zeisel, A. et al. Molecular architecture of the mouse nervous system. *Cell* **174**, 999–1014 (2018).
30. Boisvert, M. M., Erikson, G. A., Shokhirev, M. N. & Allen, N. J. The aging astrocyte transcriptome from multiple regions of the mouse brain. *Cell Rep.* **22**, 269–285 (2018).
31. Batiuk, M. Y. et al. Identification of region-specific astrocyte subtypes at single cell resolution. *Nat. Commun.* **11**, 1220 (2020).
32. Allen, W. E., Blosser, T. R., Sullivan, Z. A., Dulac, C. & Zhuang, X. Molecular and spatial signatures of mouse brain aging at single-cell resolution. *Cell* **186**, 194–208 (2023).
33. De Bastiani, M. A. et al. Hippocampal GFAP-positive astrocyte responses to amyloid and tau pathologies. *Brain Behav. Immun.* **110**, 175–184 (2023).
34. Dehkordi, S. K. et al. Profiling senescent cells in human brains reveals neurons with CDKN2D/p19 and tau neuropathology. *Nat. Aging* **1**, 1107–1116 (2021).
35. Lange, M. et al. CellRank for directed single-cell fate mapping. *Nat. Methods* **19**, 159–170 (2022).
36. Van Hoesen, G. W., Hyman, B. T. & Damasio, A. R. Entorhinal cortex pathology in Alzheimer's disease. *Hippocampus* **1**, 1–8 (1991).
37. Kobayashi, E. et al. Activated forms of astrocytes with higher GLT-1 expression are associated with cognitive normal subjects with Alzheimer pathology in human brain. *Sci. Rep.* **8**, 1712 (2018).
38. Ortinski, P. I. et al. Selective induction of astrocytic gliosis generates deficits in neuronal inhibition. *Nat. Neurosci.* **13**, 584–591 (2010).
39. Funkhouser, E. B. The visual cortex, its localization, histological structure, and physiological function. *J. Exp. Med.* **21**, 617–628 (1915).
40. Köhler, S., Winkler, U. & Hirrlinger, J. Heterogeneity of astrocytes in grey and white matter. *Neurochem. Res.* **46**, 3–14 (2021).
41. Allen, D. E. et al. Fate mapping of neural stem cell niches reveals distinct origins of human cortical astrocytes. *Science* **376**, 1441–1446 (2022).
42. Montal, V. et al. Network Tau spreading is vulnerable to the expression gradients of *APOE* and glutamatergic-related genes. *Sci. Transl. Med.* **14**, eabn7273 (2022).

43. Noori, A., Mezlini, A. M., Hyman, B. T., Serrano-Pozo, A. & Das, S. Systematic review and meta-analysis of human transcriptomics reveals neuroinflammation, deficient energy metabolism, and proteostasis failure across neurodegeneration. *Neurobiol. Dis.* **149**, 105225 (2021).
44. Noori, A., Mezlini, A. M., Hyman, B. T., Serrano-Pozo, A. & Das, S. Differential gene expression data from the human central nervous system across Alzheimer's disease, Lewy body diseases, and the amyotrophic lateral sclerosis and frontotemporal dementia spectrum. *Data Brief.* **35**, 106863 (2021).
45. Zimmer, E. R. et al. [18F]FDG PET signal is driven by astroglial glutamate transport. *Nat. Neurosci.* **20**, 393–395 (2017).
46. Salvadó, G. et al. Reactive astrogliosis is associated with higher cerebral glucose consumption in the early Alzheimer's continuum. *Eur. J. Nucl. Med. Mol. Imaging* **49**, 4567–4579 (2022).
47. March-Diaz, R. et al. Hypoxia compromises the mitochondrial metabolism of Alzheimer's disease microglia via HIF1. *Nat. Aging* **1**, 385–399 (2021).
48. Lananna, B. V. et al. *Chi3l1*/YKL-40 is controlled by the astrocyte circadian clock and regulates neuroinflammation and Alzheimer's disease pathogenesis. *Sci. Transl. Med.* **12**, eaax3519 (2020).
49. Serrano-Pozo, A., Das, S. & Hyman, B. T. APOE and Alzheimer's disease: advances in genetics, pathophysiology, and therapeutic approaches. *Lancet Neurol.* **20**, 68–80 (2021).
50. Guttenplan, K. A. et al. Neurotoxic reactive astrocytes induce cell death via saturated lipids. *Nature* **599**, 102–107 (2021).
51. La Joie, R. et al. Prospective longitudinal atrophy in Alzheimer's disease correlates with the intensity and topography of baseline tau-PET. *Sci. Transl. Med.* **12**, eaau5732 (2020).
52. Galea, E. et al. Multi-transcriptomic analysis points to early organelle dysfunction in human astrocytes in Alzheimer's disease. *Neurobiol. Dis.* **166**, 105655 (2022).
53. Viejo, L. et al. Systematic review of human post-mortem immunohistochemical studies and bioinformatics analyses unveil the complexity of astrocyte reaction in Alzheimer's disease. *Neuropathol. Appl. Neurobiol.* **48**, e12753 (2022).
54. Serrano-Pozo, A., Gómez-Isla, T., Growdon, J. H., Frosch, M. P. & Hyman, B. T. A phenotypic change but not proliferation underlies glial responses in Alzheimer disease. *Am. J. Pathol.* **182**, 2332–2344 (2013).
55. Serrano-Pozo, A. et al. Differential relationships of reactive astrocytes and microglia to fibrillar amyloid deposits in Alzheimer disease. *J. Neuropathol. Exp. Neurol.* **72**, 462–471 (2013).
56. Serrano-Pozo, A., Betensky, R. A., Frosch, M. P. & Hyman, B. T. Plaque-associated local toxicity increases over the clinical course of Alzheimer disease. *Am. J. Pathol.* **186**, 375–384 (2016).
57. Muñoz-Castro, C. et al. Cyclic multiplex fluorescent immunohistochemistry and machine learning reveal distinct states of astrocytes and microglia in normal aging and Alzheimer's disease. *J. Neuroinflammation* **19**, 30 (2022).
58. Burda, J. E. et al. Divergent transcriptional regulation of astrocyte reactivity across disorders. *Nature* **606**, 557–564 (2022).

Methods

Human specimens

Frozen (−80 °C) brain specimens from 32 participants were obtained from the Massachusetts Alzheimer's Disease Research Center (MADRC) Brain Bank, including 11 Braak NFT stages 0/I/II (B1), five Braak NFT stages III/IV (B2) and 16 Braak NFT stages V/VI (B3). Donors or their next-of-kin provided written informed consent for the brain donation, and the study was performed under the MADRC Neuropathology Core Brain Bank Institutional Review Board approval (MassGeneral Brigham protocol 1999P009556). Approximately 10–20 mg of tissue from the visual cortex was homogenized (Precellys CK14 beads), RNA was extracted (MagMAX mirVana Total RNA) and RNA integrity number (RIN) was measured on a TapeStation (Agilent) to select high-quality tissue for single nuclei RNA-seq. RIN value was measured from 130 donors, of which 83 met the selected cut-off of RIN ≥ 5. Of these 83 donors, 32 were selected based on neuropathological criteria and tissue availability. RIN values were additionally measured from the EC, BA20, BA46, V2 and V1 pieces used for snRNA-seq. The following five brain regions were chosen based on Braak NFT staging: EC, inferior temporal cortex (ITG, BA20), dorsolateral PFC (BA46), visual association cortex (V2, BA18/BA19) and primary visual cortex (V1, BA17). The cortex was carefully dissected to exclude the underlying white matter, ensuring only the cortex was included. Donors were selected based on their global AD neuropathological burden, and no randomization was performed. No statistical methods were used to predetermine sample sizes, but our sample sizes are similar to those reported in previous publications[9–17]. No donors or samples were excluded from the analysis. Data collection and analysis were not performed blind to neuropathological diagnosis.

Nuclei isolation and sorting

Nuclei were isolated and sorted following published procedures[18]. Briefly, 30–40 (40 µm thick) cryostat sections were lysed in a sucrose lysis buffer (10 mM Tris–HCl (pH 8.0), 320 mM sucrose, 5 mM $CaCl_2$, 3 µM $Mg(Ac)_2$, 0.1 mM EDTA, 1 mM DTT and 0.1% Triton X-100). The resulting lysates were filtered through a 70 µm pore cell strainer, and nuclei were purified from filtrates by ultracentrifugation (107,000*g* for 1.5 h at 4 °C) through a sucrose cushion (10 mM Tris–HCl (pH 8.0), 1.8 M sucrose, 3 µM $Mg(Ac)_2$, 0.1 mM EDTA and 1 mM DTT). Supernatants were removed, and pellets were resuspended in 2% BSA/PBS containing RNase inhibitor (0.2 U μl^{-1}; Roche). To enrich astrocyte nuclei, we followed a strategy of depletion of neurons and oligodendrocytes. Nuclei were labeled with Alexa Fluor 647-conjugated mouse monoclonal anti-NeuN antibody (clone 1B7; Novus Biologicals, NBP1-92693AF647) and PE-conjugated mouse monoclonal anti-OLIG2 antibody (clone 211F1.1; EMD Millipore, MABN50A4). After washes, nuclei were stained with Sytox blue (Thermo Fisher Scientific) and sorted on a BD FACSAria Fusion. For each sample, we collected $Sytox^{pos}NeuN^{pos}OLIG2^{neg}$ and $Sytox^{pos}NeuN^{neg}OLIG2^{neg}$.

snRNA-seq library construction and sequencing

Single-nucleus cDNA libraries were constructed using the Chromium Single-Cell 3′ Reagents Kit V3 following the manufacturer's instructions (10x Genomics). Samples were pooled and sequenced targeting at least 30K reads per cell on a HiSeq 2000 (Illumina). Separation of $NeuN^{pos}OLIG2^{neg}$ and $NeuN^{neg}OLIG2^{neg}$ into unique libraries allowed for an increased number of reads and detected genes in nonneuronal cells as compared to published studies containing nonenriched nuclei (Supplementary Fig. 1a).

pTau and tau ELISA

Protein extracts were prepared from frozen tissue adjacent to that used for snRNA-seq by homogenizing in PBS and centrifuging at 3,000*g* for 10 min at 4 °C. The resulting supernatants were subjected to ELISA for total tau and tau phosphorylated at Threonin-231 using the MesoScale Discovery (MSD) Phospho(Thr231)/Total Tau Kit (MSD, K15121D) according to the manufacturer's instructions. The plates were developed using the MESO QuickPlex SQ120 Plate Reader (MSD). Total tau and phosphorylated tau concentrations were determined using the calibration curve and the pTau/total tau ratio was estimated.

Immunohistochemistry and quantitative analyses on postmortem brain sections

For Aβ immunohistochemistry, frozen cryostat sections adjacent to those used for snRNA-seq were subjected to immunohistochemistry with the mouse monoclonal anti-N-terminal Aβ antibody clone 3D6. The staining was performed on a Leica BOND Rx automated stainer using DAB-based detection (Leica). Sections were scanned in a slide scanner (Pannoramic 250, 3DHistech), and area fraction (that is, the percentage area of tissue section occupied by 3D6-immunoreactive plaques) was measured using HALO software (Indica Labs).

AQP4 and connexin-43 (gene name *GJA1*) immunoreactive area fractions were measured on formalin-fixed paraffin-embedded sections of the EC and occipital cortex of $n = 11$ control donors (including two donors of the present snRNA-seq study as EC paraffin blocks were not available for the remaining six pathology stage 1 donors), which were stained on a Leica BOND Rx automated stainer using DAB-based detection and hematoxylin counterstaining, followed by scanning at 40× on a VS120 Olympus slide scanner (Olympus). Area fraction was obtained using the open access software QuPath (v.0.3.2.)[59]. Briefly, the EC and V1 regions were carefully outlined with the guidance of the Allen Adult Human Reference Brain Atlas (https://atlas.brain-map.org), and AQP4 and connexin-43 area fractions were obtained with the pixel classifier and threshold tools, respectively. Within-donor comparisons between EC and V1 for each marker were performed with a two-tailed paired *t* test with a statistical significance level of $P < 0.05$.

For multiplex fluorescence immunohistochemistry validation studies, 7-µm-thick formalin-fixed paraffin-embedded sections from the contralateral brain hemisphere of the same donors were dewaxed in xylenes, rehydrated in decreasing concentrations of ethanol and subjected to antigen retrieval (microwaved in boiling citrate buffer 0.1 M (pH 6.0), with 0.05% Tween-20 at 95 °C for 20 min), followed by blocking with 10% normal donkey serum in TBS for 1 h at room temperature. Primary antibodies (Supplementary Data 8) were incubated in 5% normal donkey serum in TBS overnight at 4 °C. Fluorescently labeled secondary antibodies were incubated in 5% normal donkey serum in TBS for 2 h at room temperature. For Thioflavin-S staining, sections were incubated in Thioflavin-S 0.05% dissolved in ethanol 50% for 8 min and washed with ethanol 80% and distilled water. Slides were coverslipped with DAPI-containing mounting media (Fluoromount-G DAPI; SouthernBiotech) and scanned in a VS120 Olympus slide scanner with the same exposure time for each marker across brain regions (that is, EC versus V1) and/or diagnoses (that is, control versus AD). Multiplex fluorescence immunohistochemistry images in Figs. 2c and 5d as well as Supplementary Figs. 5, 6 and 7 have the same display settings across brain regions and diagnoses. To determine whether the expression of astrocyte reactive markers is spatially associated with Aβ plaques, plaque-centered quantitative analyses were performed in the temporal association neocortex of six donors from pathology group 1 and seven donors from pathology group 3 or 4 from the snRNA-seq sample, using QuPath. Briefly, in each AD donor, $n = 50$ Thioflavin-S-positive dense-core plaques were randomly selected and outlined throughout all layers of the cortical ribbon in the green channel being blindfolded to the expression level of the reactive astrocyte marker of interest in the red channel. Next, a 50 µm concentric halo was added to each selected plaque, and $n = 50$ regions of interest of similar size but far from any Thioflavin-S-positive plaque were added with the appropriate tools in QuPath software. For each control donor, $n = 50$ regions of interest of similar size to the AD plaques were added onto the cortical ribbon as sham plaques, together with their 50 µm halo, and $n = 50$ more regions of interest far from those sham plaques. Statistical analyses

were conducted with mixed-effects models with area fraction of the reactive marker as the dependent variable, diagnosis (control versus AD) and location (sham or Thioflavin-S-positive plaque, ≤50 µm halo, or >50 µm) as fixed effects and controlling for donor ID (random effect). Statistical significance was set at a level of $P < 0.05$.

In situ hybridization

To demonstrate *MAPT* expression in astrocytes, we performed a 3-plex fluorescence in situ hybridization on cryostat sections from the temporal association cortex and the visual association cortex (V2) of selected control and AD donors using RNAScope technology (ACD, Bio-Techne), following the manufacturer's protocol. Probes to detect human *GFAP*, *MAPT*, *SYP* (synaptophysin), *ALDH1L1 and HSPB1* mRNA (311801-C2, 408991, 311421-C3, 438881-C3 and 1045931-C1, respectively) were labeled with fluorescein, cyanine-3 or cyanine-5, respectively. Endogenous tissue autofluorescence was quenched with TrueBlack Lipofuscin Autofluorescence Quencher (Biotium). In V2 sections, fluorescence immunohistochemistry was then performed overnight with an AlexaFluor488-conjugated rabbit monoclonal anti-Aβ antibody at 1:200 in 10% normal goat serum in PBS-T (clone D52D4; Cell Signaling Technologies, 51374S) to depict Aβ plaques. Sections were imaged at ×40 magnification using an Olympus FV3000 confocal laser scanning microscope (Olympus). To quantify the ratio of *HSPB1* to *ALDH1L1* mRNA, the DAPI-positive nuclei of *ALDH1L1*-positive astrocytes were manually delineated, and the borders extended 10 µm using QuPath image analysis software. The mean intensity of both transcripts was automatically quantified within those regions.

Bioinformatics analyses

snRNA-seq processing and cell type identification. Raw reads were processed using Cell Ranger 3.0.0 (10x Genomics) with default settings, pre-mRNA package and aligned to the human GRCh38 genome. For each brain region, we removed cells with fewer than 200 genes, greater than 20,000 unique molecular identifiers (UMIs) and/or greater than 15% mitochondrial genes, and used reciprocal principal component analysis (rPCA) integration based on the top 2,000 highly variable genes (HVGs) to remove donor-specific effects using the Seurat R package (v.4.3.0)[60]. For the clustering of nuclei, integrated gene expression data were log-normalized, scaled and subjected to PCA to choose the number of principal components for clustering, which was followed by nonlinear dimensionality reduction via UMAP and visualized with UMAP plots. Next, nuclei from various cell types were annotated based on the relative expression levels of known genes. Astrocyte nuclei were identified by their high expression of *ADGRV1*, *ALDH1L1*, *AQP4* and *GFAP*.

The following filters were applied to select the genes and astrocyte nuclei for downstream analyses: (1) 18,283 protein-coding genes (that is, noncoding genes were excluded), (2) genes with the sum of counts >100 in at least 30% of samples (for example, $n = 11{,}148$ for BA20), and (3) nuclei with <25,000 UMIs after gene filtering (to exclude multiplets) and >2,000 genes detected (that is, with a count >0; for example, $n = 70{,}984$ nuclei for BA20). After filtering, a second round of integration was performed via canonical correlation analysis to regress out donor-specific effects as well as the percentage of mitochondrial genes.

Analysis of normal aging brains. Nuclei from control brains were integrated by rPCA and clustered using FindClusters from the Seurat package at 0.4 resolution. Markers for each cluster were identified using FindAllMarkers from the Seurat package, and functional enrichment of clusters was performed against the MSigDB database[61] using a hypergeometric test. Differential expression of each brain region relative to other regions was also performed using FindAllMarkers. DEGs that pass the average fold change (FC) cut-off (FC > 1.2 for upregulated genes and FC < 0.8 for the downregulated genes), had an adjusted P value < 0.05 and were expressed in greater than 50% of the cells in the given brain region are reported. To find associations of gene expression with pTau pathology, we used Model-based Analysis of Single-cell Transcriptomics (MAST)[62] to perform zero-inflated regression analysis by fitting a mixed model. The model specification was as follows:

$$\mathrm{zlm}(\sim \mathrm{pTau/Tau} + (1|\mathrm{donor/sample}) + \mathrm{cngeneson} + \mathrm{pc}_{\mathrm{mito}}, \mathrm{sca}, \mathrm{method} = ''\mathrm{glmer}'', \mathrm{ebayes} = F),$$

where cngeneson is the cellular detection rate and pc_mito is the percentage of counts mapping to mitochondrial genes.

Identification of gene sets following distinct spatial and temporal trajectories. To identify gene sets that followed distinct spatial trajectories along the neural network, we first performed a differential expression analysis comparing each node of the network with the next (that is, EC versus ITG, ITG versus PFC, PFC versus V2 and V2 versus V1) using FindMarkers with DonorID and Pathology Stage as latent variables. We selected DEGs that were log(FC) > 0.25, adjusted $P < 0.05$ and percentage expression greater than 10% in both regions. Next, to describe the spatial gene patterns, we calculated the standardized gene expression score scaling across brain regions for each donor and then averaged those across all donors for each brain region. The resulting mean standardized gene expression scores were grouped into six gene sets by spectral clustering using SNFTool (v.2.3.1)[63] with $k = 6$. To find the overlap with the EC/V1 high or low genes, we used a hypergeometric test. To compute the association of the gene sets with Aβ and pTau/tau local measures, we used a mixed-effects model:

$$\mathrm{mean}_{\mathrm{trend}} \sim (1|\mathrm{donorID}) + A\beta\mathrm{OR}\ \mathrm{pTau/tau}$$

For the temporal gene patterns, we similarly performed a differential expression analysis comparing two adjacent pathology stages (stage 2 versus stage 1, stage 3 versus stage 2 and stage 4 versus stage 3), using FindMarkers with Region as a latent variable. We selected DEGs that were log(FC) > 0.25, adjusted $P < 0.05$ and percentage expression greater than 10% in both regions. We then computed the standardized gene expression scores by scaling across all the samples for a gene and then computed the average standardized gene expression score for each pathology stage. The resulting scores were similarly used as input for the spectral clustering using SNFTool (v.2.3.1)[63] with $k = 6$.

Identification of astrocyte subclusters. For clustering, we randomly sampled 500 astrocyte nuclei from each sample (that is, each donor and region; total $n = 70{,}551$). The concatenated count matrix of subsampled cells was normalized and log transformed via Seurat (v.4.3.0)[60]. The top 2,000 HVGs, identified using the vst method in the FindVariableFeatures function, were selected for the principal component analysis. Batch effects due to technical variation were corrected using the RunHarmony function in Harmony (v.0.1.1) package[64], with the top 20 principal components as input. Clustering and UMAP projections were performed in Seurat using the Harmony data. Cell density estimations of astrocyte subclusters across each region and stage were performed using the stat_density_2d function in the ggplot2 (v.3.4.2) package. The effects of factors such as age and sex on cell subcluster frequency across samples were modeled using multiple linear regression with the formula: frequency ~1 + pTau/tau + region + sex + age + pTau/tau × sex + pTau/tau × region.

Pseudotime analysis. Pseudotime analysis was conducted using the monocle3 (v.1.3.1) package[65]. With the pregenerated UMAP locations of sampled cells, a principal graph was learned through the UMAP using the learn_graph function. Then the pseudotime value for each cell was calculated based on the principal graph using the order_cells function. We set astH0 as the root node of the principal graph by the get_earliest_principal_node function. DEGs across the trajectory were

identified by the graph_test function and were presented on a heatmap along the pseudotime.

RNA velocity analysis. Spliced and unspliced reads of each sample were counted by velocyto[66] Python implementation (v.0.17.17) based on previously aligned BAM files of the snRNA-seq reads data. Then, the calculation of RNA velocity for each gene in each cell was implemented by following the scVelo[67] (v.0.3.1) pipeline under dynamics mode. We then applied the differential_kinetic_test function to test for differential kinetics across subclusters of the top 100 fit-likelihood genes and recomputed velocity with diff_kinetics = True under dynamics mode. The velocity was then used as input for CellRank[35] (v.2.0.2) to construct a custom kernel that combined the velocity kernel with the connectivity kernel and monocle3-based pseudotime kernel at a ratio of 80%, 10% and 10%, respectively. The velocity embedding stream was estimated by this combined kernel.

Comparison with other public datasets. We performed label transfer to compare our dataset with astrocytes from nine public astrocyte-containing snRNA-seq datasets. For each dataset, we downloaded the count matrix and metadata, randomly subsampled 500 astrocyte cells from each sample, removed low-quality cells with mitochondrial percentages larger than 5%, normalized with the SCTransform(vars.to.regress = c('percent.mt', 'Sample ID')) function and *RunPCA* analysis in Seurat (v.4.3.0)[60]. We then identified anchors with the FindTransferAnchors function using the present study dataset as a reference and every other public dataset as a query. TransferData and MapQuery functions with identified anchors were used to predict labels of cells in the query dataset and map query cells to the reference UMAP. The predicted labels were used to calculate the proportion of each subcluster within the samples. The significance of differences in subcluster proportions between groups in each study was evaluated using a two-sided Welch's *t* test and adjusted with the Benjamini–Hochberg method. Normality for each group was assessed using the Shapiro–Wilk test, and equal variances were not assumed.

To compare the present study subcluster marker gene sets with those from public datasets, we manually curated highlighted gene sets in public papers, then analyzed overrepresentation between gene sets with newGOM function in the GeneOverlap package (v.1.30.0). *P* values were corrected with Benjamin–Hochberg's correction.

Reporting summary

Further information on research design is available in the Nature Portfolio Reporting Summary linked to this article.

Data availability

The snRNA-seq dataset generated for the study will be made available at Gene Expression Omnibus (GEO: GSE268599) and Sequence Read Archive (PRJNA916657) upon acceptance of the paper. Genes and pathways information is available in Supplementary Data 1–8. Data can also be queried via the interactive web application at https://ad-progression-atlas.partners.org/. The processed single-cell gene expression data and metadata can also be downloaded directly from the website. Other datasets used in this study can be found in the Synapse, GEO or custom public repositories as follows: ref. 9, syn18485175; ref. 10, GSE138852; ref. 13, GSE157827; ref. 11, syn21125841; ref. 12, GSE147528; ref. 15, GSE160936; ref. 14, GSE167494; ref. 16, GSE243292 and Seattle-AD, https://portal.brain-map.org/explore/seattle-alzheimers-disease. The findings of the present study are available at https://ad-progression-atlas.partners.org.

Code availability

All codes generated during this study are accessible at https://github.com/mindds/ad-progression-study (https://doi.org/10.5281/zenodo.13315411).

References

59. Bankhead, P. et al. QuPath: open source software for digital pathology image analysis. *Sci. Rep.* **7**, 16878 (2017).
60. Hao, Y. et al. Integrated analysis of multimodal single-cell data. *Cell* **184**, 3573–3587 (2021).
61. Liberzon, A. et al. Molecular signatures database (MSigDB) 3.0. *Bioinformatics* **27**, 1739–1740 (2011).
62. Finak, G. et al. MAST: a flexible statistical framework for assessing transcriptional changes and characterizing heterogeneity in single-cell RNA sequencing data. *Genome Biol.* **16**, 278 (2015).
63. Wang, B. et al. Similarity network fusion for aggregating data types on a genomic scale. *Nat. Methods* **11**, 333–337 (2014).
64. Korsunsky, I. et al. Fast, sensitive and accurate integration of single-cell data with Harmony. *Nat. Methods* **16**, 1289–1296 (2019).
65. Qiu, X. et al. Single-cell mRNA quantification and differential analysis with Census. *Nat. Methods* **14**, 309–315 (2017).
66. La Manno, G. et al. RNA velocity of single cells. *Nature* **560**, 494–498 (2018).
67. Bergen, V., Lange, M., Peidli, S., Wolf, F. A. & Theis, F. J. Generalizing RNA velocity to transient cell states through dynamical modeling. *Nat. Biotechnol.* **38**, 1408–1414 (2020).

Acknowledgements

We would like to thank the patients and families involved in research at the MADRC. The results published here are in whole or in part based on data obtained from the AD Knowledge Portal (https://adknowledgeportal.org). We also thank P. Dooley from the MADRC brain bank for technical support. We acknowledge funding from the following sources: National Institutes of Health/National Institute on Aging (P30AG062421 to B.T.H., S.D. and A.S.-P.; 5K08AG064039 to A.S.-P.), Alzheimer's Association (AACF-17-524184 and AACF-17-524184-RAPID to A.S.-P.), Real Colegio Complutense at Harvard University Research Fellowship (to C.M.-C.), Prince Mahidol Award Youth Program Research Scholarship (to M.J.) and Massachusetts Life Sciences Center Neuroscience Consortium award (to S.D., Z.L. and H.L.).

Author contributions

A.S.-P., B.T.H., R.E.B. and S.D. conceived the study and designed experiments, and together with H.L. and Z.L., they designed and conducted the bioinformatics analyses. T.R.C. assisted in brain donor selection and dissected the brain samples. M.E.W. led the protocol development for snRNA-seq from the human brain. T.P. performed nuclei isolation. M.E.W. performed FANS. J.T. and A.A. generated the snRNA-seq libraries. K.Z. and F.L. quantified the Aβ plaque burden. M.H. performed the pTau/tau ELISAs. C.M.-C., M.J. and M.A.H. performed the fluorescence immunohistochemistry validation. L.A.W. performed the RNAScope validation. R.J.,. A.B., A.W., T.K. and G.L. contributed to the analyses. A.N. developed the shiny web interface. B.T.H., K.B., R.V.T. and E.K. acquired funding and initiated the study. A.S.-P. and S.D. wrote the manuscript. M.E.W., R.E.B., H.L. and Z.L. contributed to the methods. All authors approved of and contributed to the final version of the manuscript.

Competing interests

M.E.W., A.W., K.Z., F.L., G.L., T.P., J.T., A.A., T.K., R.V.T, K.B. and E.H.K. are employees of Abbvie. The design, study conduct and financial support for this research were provided by Abbvie. Abbvie participated in the interpretation of data, review and approval of the publication. B.T.H. has a family member who works at Novartis and owns stock in Novartis, serves on the scientific advisory board of Dewpoint and owns stock, serves on a scientific advisory board or is a consultant for Abbvie, Arvinas, Biogen, Novartis, Cell Signaling Technologies, Sangamo, Sanofi, Takeda, US Department of Justice and Vigil, and his laboratory is supported by sponsored research agreements with Abbvie, F Prime and Spark. The remaining authors declare no competing interests.

Additional information

Supplementary information The online version contains supplementary material available at https://doi.org/10.1038/s41593-024-01791-4.

Correspondence and requests for materials should be addressed to Sudeshna Das.

Peer review information *Nature Neuroscience* thanks the anonymous reviewers for their contribution to the peer review of this work.

nature portfolio

Corresponding author(s): Sudeshna Das

Last updated by author(s): August 16, 2024

Reporting Summary

Nature Portfolio wishes to improve the reproducibility of the work that we publish. This form provides structure for consistency and transparency in reporting. For further information on Nature Portfolio policies, see our Editorial Policies and the Editorial Policy Checklist.

Statistics

For all statistical analyses, confirm that the following items are present in the figure legend, table legend, main text, or Methods section.

n/a	Confirmed
☐	☒ The exact sample size (*n*) for each experimental group/condition, given as a discrete number and unit of measurement
☐	☒ A statement on whether measurements were taken from distinct samples or whether the same sample was measured repeatedly
☐	☒ The statistical test(s) used AND whether they are one- or two-sided *Only common tests should be described solely by name; describe more complex techniques in the Methods section.*
☐	☒ A description of all covariates tested
☐	☒ A description of any assumptions or corrections, such as tests of normality and adjustment for multiple comparisons
☐	☒ A full description of the statistical parameters including central tendency (e.g. means) or other basic estimates (e.g. regression coefficient) AND variation (e.g. standard deviation) or associated estimates of uncertainty (e.g. confidence intervals)
☐	☒ For null hypothesis testing, the test statistic (e.g. *F*, *t*, *r*) with confidence intervals, effect sizes, degrees of freedom and *P* value noted *Give P values as exact values whenever suitable.*
☒	☐ For Bayesian analysis, information on the choice of priors and Markov chain Monte Carlo settings
☒	☐ For hierarchical and complex designs, identification of the appropriate level for tests and full reporting of outcomes
☒	☐ Estimates of effect sizes (e.g. Cohen's *d*, Pearson's *r*), indicating how they were calculated

Our web collection on statistics for biologists contains articles on many of the points above.

Software and code

Policy information about availability of computer code

Data collection	No data collection software was used.
Data analysis	The code for all data analyses is available on GitHub: https://github.com/mindds/ad-progression-study/ All analysis was conducted in R version 4.0.2 (2020-06-22) and Python 3.8.5 with the following packages. CellRank v.2.0.22 GeneOverlap v.1.30.0 Harmony v.0.1.1 MAST monocle3 v.1.3.1 scVelo v.0.3.1 Seurat v.4.3.0 SNFtool v.2.3.1 velocyto v.0.17.17

For manuscripts utilizing custom algorithms or software that are central to the research but not yet described in published literature, software must be made available to editors and reviewers. We strongly encourage code deposition in a community repository (e.g. GitHub). See the Nature Portfolio guidelines for submitting code & software for further information.

Data

Policy information about availability of data

All manuscripts must include a data availability statement. This statement should provide the following information, where applicable:

- Accession codes, unique identifiers, or web links for publicly available datasets
- A description of any restrictions on data availability
- For clinical datasets or third party data, please ensure that the statement adheres to our policy

The snRNA-seq dataset generated for the study are available at GEO and SRA (GEO: GSE268599 and SRA: PRJNA916657). Genes and pathways information are available as Supplementary Tables. Data can also be queried via the interactive web application at https://ad-progression-atlas.partners.org. The processed single-cell gene expression data and metadata can also be downloaded directly from the website.

Other datasets used in this study be found in the Synapse, GEO, or custom public repositories as follows: Mathys et al., syn18485175; Grubman et al., GSE138852; Lau et al., GSE157827; Zhou et al., syn21125841; Leng et al., GSE147528; Smith et al., GSE160936, Sadick et al., GSE167494; Dai et al., GSE243292; and Seattle-AD, https://portal.brain-map.org/explore/seattle-alzheimers-disease/

Human research participants

Policy information about studies involving human research participants and Sex and Gender in Research.

Reporting on sex and gender	Sex was ascertained at autopsy. There were 19 females and 13 males included in this study. Given n=32 with a wide range of Alzheimer's disease neuropathological changes, differences in gene expression by sex were not investigated. Gender was not ascertained or used as co-variate in this study.
Population characteristics	n=32 donors, 19 females and 13 males, with an age range 58-90+, various degrees of Alzheimer's disease neuropathological changes (i.e., Braak NFT stage 0/I/II n=11; III n=5; V n=8; and VI n=8), and APOE genotype distribution e2/e2 n=1, e2/e3 n=2, e3/e3 n=22, e3/e4 n=6, e4/e4 n=1, e4/e4 n=1.
Recruitment	Subjects are recruited either through the Clinical Core of the Massachusetts Alzheimer Disease Research Center (MADRC) or by conversations with their physicians about the possibility of brain donation.
Ethics oversight	Donors or their next-of-kin provided written informed consent for the brain donation and the study was performed under the MADRC Neuropathology Core Brain Bank Institutional Review Board approval (MassGeneral Brigham protocol #1999P009556). No compensation was provided to the participants for the brain donation.

Note that full information on the approval of the study protocol must also be provided in the manuscript.

Field-specific reporting

Please select the one below that is the best fit for your research. If you are not sure, read the appropriate sections before making your selection.

☒ Life sciences ☐ Behavioural & social sciences ☐ Ecological, evolutionary & environmental sciences

For a reference copy of the document with all sections, see nature.com/documents/nr-reporting-summary-flat.pdf

Life sciences study design

All studies must disclose on these points even when the disclosure is negative.

Sample size	N=32. No statistical methods were used to predetermine sample sizes, but our sample sizes are similar to those reported in previous publications. No donors or samples were excluded from the analysis. Sample collection and analysis were not performed blind to the neuropathological diagnosis.
Data exclusions	Pre-specified exclusion criteria were (1) Primary neuropathological diagnosis other than "normal brain" or "Alzheimer's disease neuropathological changes;" (2) RNA Integrity Number (RIN) <5; and (3) tissue not available.
Replication	No replication was attempted.
Randomization	The study participants were allocated into pathology stages based on the overall AD neuropathology.
Blinding	Data collection and analysis were not performed blind to the conditions of the experiments.

Reporting for specific materials, systems and methods

We require information from authors about some types of materials, experimental systems and methods used in many studies. Here, indicate whether each material, system or method listed is relevant to your study. If you are not sure if a list item applies to your research, read the appropriate section before selecting a response.

Materials & experimental systems

n/a	Involved in the study
☐	☒ Antibodies
☒	☐ Eukaryotic cell lines
☒	☐ Palaeontology and archaeology
☒	☐ Animals and other organisms
☒	☐ Clinical data
☒	☐ Dual use research of concern

Methods

n/a	Involved in the study
☒	☐ ChIP-seq
☒	☐ Flow cytometry
☒	☐ MRI-based neuroimaging

Antibodies

Antibodies used

Mouse anti-Aldehyde dehydrogenase 1 L1 monoclonal antibody, Millipore, Cat#MABN495, clone N103/39, RRID AB_2687399, 1:500
Rabbit anti-Aquaporin-1 polyclonal antibody, Millipore, Cat#AB2219, RRID AB_1163380, 1:500
Rabbit anti-Aquaporin-4 C-terminus polyclonal antibody, Millipore, Cat#AB3594, RRID AB_91530, 1:500 (fluorescence), 1:10,000 (DAB)
Rabbit anti-Cluster of differentiation 44 monoclonal antibody, Ventana-Roche, Cat#790-4537, clone SP37, RRID not available, undiluted
Rabbit anti-alpha-B-Crystallin polyclonal antibody, Millipore, Cat#ABN185, RRID AB_11213811, 1:500
Rabbit anti-Glial fibrillary acidic protein polyclonal antibody, Sigma-Aldrich, Cat#G9269, RRID AB_477035, 1:1,000
Mouse anti-Glial fibrillary acidic protein monoclonal antibody, Sigma-Aldrich, Cat#G3893, clone G-A-5, RRID AB_477010, 1:1,000
Rabbit anti-Connexin-43 polyclonal antibody, Cell Signaling Technologies, Cat#3512, RRID AB_2294590, 1:500 (fluorescence), 1:50 (DAB)
Mouse anti-Glutamine synthetase monoclonal antibody, Millipore, Cat#MAB302, clone GS-6, RRID AB_2110656, 1:500
Rabbit anti-Heat shock protein 27 kDa monoclonal antibody, Cell Signaling Technologies, Cat#95357, clone D6W5V, RRID AB_2800246, 1:250
Rabbit anti-Monoamine oxidase B monoclonal antibody, Abcam, Cat#ab133270, clone EPR7102, RRID AB_11157541, 1:500
Rabbit anti-Excitatory amino acid transporter 2 polyclonal antibody, Proteintech, Cat#22515-1-AP, RRID AB_2879112, 1:50
Rabbit anti-Excitatory amino acid transporter 1 polyclonal antibody, Abcam, Cat#ab416, RRID AB_304334, 1:100

Validation

Mouse anti-Aldehyde dehydrogenase 1 L1 monoclonal antibody, rabbit anti-Glial fibrillary acidic protein polyclonal antibody, mouse anti-Glutamine synthetase monoclonal antibody, rabbit anti-Excitatory amino acid transporter 1 polyclonal antibody, and the rabbit anti-Monoamine oxidase B monoclonal antibody were validated by the authors in prior papers (Muñoz-Castro C et al. J Neuroinflam 2022; 19(1): 30, PMID: 35109872; Serrano-Pozo A et al. Am J Pathol 2013; 182(6); 2332-44, PMID: 23602650, Jaisa-Aad M et al., Acta Neuropathol. 2024, 147(1):66. PMID: 38568475). The anti- CD44, CX43, AQP1, AQP4, HSP27, and alpha-B-Crystallin antibodies were demonstrated to label GFAP+ astrocytes in double fluorescent immunohistochemistry. The rabbit anti-alpha-B-Crystallin polyclonal antibody and the rabbit anti-Heat shock protein 27 kDa monoclonal antibody also labeled some neurons and oligodendrocytes.